Research Square

Preprints are preliminary reports that have not undergone peer review.
They should not be considered conclusive, used to inform clinical practice,
or referenced by the media as validated information.

Biomimetic Tryptophan-derived Carbon Dots as Nano-inhibitors to Reprogram Tryptophan-IDO1 Metabolic Axis for Peripheral Nerve Regeneration

Xin Yu
First Hospital of Jilin University
Jingyan Ren
First Hospital of Jilin University
Zhenghang Li
First Hospital of Jilin University
Wenjun Yu
First Hospital of Jilin University
Jie Zhang
First Hospital of Jilin University
Deer Yi
First Hospital of Jilin University
Qidong Shi
First Hospital of Jilin University
Laijin Lu
First Hospital of Jilin University
Bin Liu
First Hospital of Jilin University
Mingxi Yang
yangmxchem@jlu.edu.cn

First Hospital of Jilin University

Research Article

Keywords: peripheral nerve injury, Schwann cells, tryptophan metabolism, carbon dots, IDO1inhibitors, lipophagy

Posted Date: November 10th, 2026

DOI: https://doi.org/10.21203/rs.3.rs-11487095/v1

License: This work is licensed under a Creative Commons Attribution 4.0 International License.
Read Full License

Additional Declarations: No competing interests reported.

Biomimetic Tryptophan-derived Carbon Dots as Nano-inhibitors to Reprogram Tryptophan-IDO1 Metabolic Axis for Peripheral Nerve Regeneration

Xin Yu[a,c,d], Jingyan Ren[a,c,d], Zhenghang Li[a,c,d], Wenjun Yu[a], Jie Zhang[a,c,d], Deer Yi[a,c,d], Qidong Shi[e], Laijin Lu[a,c,d], Bin Liu[a,c,d,**], MingXi Yang[a,b,d,*]

[a] Department of Hand and Podiatric Surgery, Orthopedics Center, The First Hospital of Jilin University, Jilin University, Changchun 130031, PR China

[b] Orthopedics Central Laboratory, Institute of Translational Medicine, The First Hospital of Jilin University, Jilin University, Changchun 130021, PR China

[c] Jilin Provincial Clinical Medical Research Center of Hand and Foot Surgery, The First Hospital of Jilin University, Jilin University, Changchun 130021, PR China

[d] Key Laboratory of Tissue Repair, Reconstruction and Regeneration of Jilin Province, The First Hospital of Jilin University, Jilin University, Changchun 130021, PR China

[e] Department of Cardiovascular Medicine, The First Hospital of Jilin University, Jilin University, Changchun 130021, PR China

[*] Corresponding author:

Mingxi Yang

E-mail: yangmxchem@jlu.edu.cn

[**] Corresponding author:

Bin Liu

E-mail: l_bin@jlu.edu.cn

Abstract

Peripheral nerve injury (PNI) remains a challenge in clinic with limited therapeutic options, where pathological disturbance of glial cells severely impedes axonal regeneration and functional recovery. Herein, the tryptophan (TRP)/indoleamine 2,3-dioxygenase 1 (IDO1)/kynurenine (KYN) metabolic axis was clarified to trigger Schwann cells (SCs) dysfunction by depletion of neuroprotective 5-hydroxytryptamine and accumulation of neurotoxic quinolinic acid. To rectify this abnormal metabolism, for the first time, we proposed a TRP-heritable mimicry (THM) strategy, and a series of biomimetic tryptophan-derived carbon dots (TNDs) were synthesized through mild non-enzymatic catalytic oxidation and Schiff-base reaction, which retained the enzyme recognition groups of TRP but not involved in TRP metabolism. Specifically, an estimated 2.83-fold higher binding affinity for IDO1 than free TRP was achieved by Li^+-doped TNDs (TLNDs), which could effectively redirect TRP metabolic flux, activate NRF2-HO1 antioxidant axis in SCs with an IDO1-dependent manner, indicating that TLNDs could serve as a competitive IDO1 nano-inhibitor. Moreover, the TLNDs preferentially accumulated in lysosomes upon lipid raft-mediated endocytosis, where acid-responsive released Li^+ stimulated SCs autophagy and enhanced TFEB-mediated lysosomal biogenesis to accelerate lipophagy and cholesterol transport. In a rat sciatic nerve crush model, subepineurial TLNDs injection significantly suppressed neuroinflammation, promoted myelination, and ultimately led to favorable motor function recovery. This study identified IDO1-mediated TRP metabolic reprogramming as a critical PNI therapeutic target and provided a novel carrier-free specific IDO1-inhibition strategy for synergistic metabolic regulation and SCs functional activation to boost nerve regeneration, which also presented broad prospects in the field of central nervous system disease.

Keywords: peripheral nerve injury; Schwann cells; tryptophan metabolism; carbon dots; IDO1inhibitors; lipophagy

1. Introduction

Peripheral nerve injury (PNI) is a prevalent and debilitating traumatic event worldwide, resulting not only in severe disabilities but also imposing a significant economic burden [1-3]. Recent studies primarily focus on axonal guidance and regenerative microenvironment following PNI, while one critical aspect that has been largely overlooked is supportive metabolic dysfunction of Schwann cells (SCs) [4-6]. Nerve injury breaks mitochondrial and lysosomal homeostasis in SCs [7, 8], causing suppressed glial repair activity and debris clearance capability [9, 10], which are the two decisive steps in the initiation of nerve regeneration [11, 12]. Relieving single organelle damage often fails to prevent the detrimental cycle of prolonged energy supply disorders and myelin lipid metabolic stress.

Tryptophan (TRP) serves as a significant modulator of neuronal homeostasis in the central and peripheral nervous system. The two core metabolic axes of TRP, i.e., 5-hydroxytryptamine (5-HT) pathway and kynurenine (KYN) pathway, are responsible for neurotransmitter secretion and inflammation/immune regulation, respectively, competing for TRP substrates and synergistically balancing neural development [13]. In this regard, Indoleamine 2,3-dioxygenase 1 (IDO1) is the primary enzyme responsible for binding and converting TRP into KYN [14]. However, after nerve injury, immune factors (IFN-γ) induce abnormal hyperactivation of IDO1, which depletes the precursors of the protective 5-HT and leads to the accumulation of toxic quinolinic acid (QUIN). The persistent and unrestrained shift of TRP metabolic pathway towards KYN has been observed in various neurological disorders, including Alzheimer's disease, ischemic stroke, and diabetic neuropathy, contributing to a cycle of neurotoxic cascade and repair obstacles [15, 16]. While TRP metabolism in the central nervous system is well documented, its regulation of mitochondrial-lysosomal homeostasis during peripheral nerve repair remains poorly investigated. Accordingly, modulation of IDO1 activity to normalize TRP metabolic axis represents a potential therapeutic target capable of rescuing impaired SCs and promoting peripheral nerve regeneration.

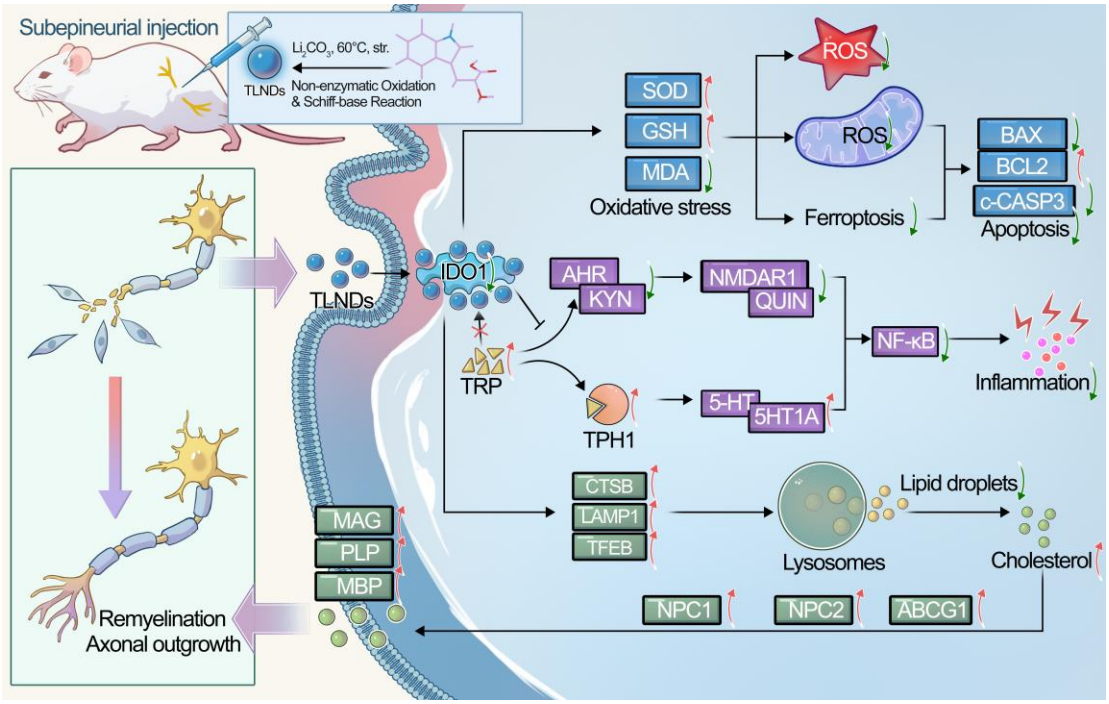
Classical small-molecule IDO1 inhibitors, such as Epacadostat (INCB 024360), IDO-IN-7 (NLG919), and 1-methyl-D-tryptophan (D-1MT, Indoximod), suppress

enzymatic activity by binding to the catalytic pocket of IDO1 [17-19], yet they face translational obstacles including weak tissue permeability, rapid systemic clearance, and off-target toxicity. Ruthenium, iridium and other metal complexes have been reported to achieve stronger binding via axial coordination with the heme sites in IDO1, thus competing with the substrate L-TRP for the active center [20], but their application is also limited by heavy metal cytotoxicity, poor water solubility, and complicated synthesis procedures. Although traditional nanocarriers such as lipids and polymers have been widely reported to encapsulate IDO1 inhibitors for tumor immune regulation [21-23], their long-term biosafety concerns and application potential in the field of nerve regeneration remain unresolved. Therefore, it is still necessary to develop a new type of carrier-free IDO1 nano-inhibitors with stronger stability and biocompatibility, and further explore the therapeutic effects and mechanisms of targeting TRP metabolism in PNI repair.

Carbon dots (CDs), a class of emerging carbon-based nanomaterials, possessed multiple advantages, including superior biocompatibility, high water dispersibility and physicochemical stability, and ease of surface modification [24]. Specifically, it is generally considered that CDs can inherit partial structural and functional features from the carbonaceous sources after carbonization [25-28]. Inspired by the concept of substrate surrogacy, we speculated that TRP can serve as a precursor to fabricate CDs that retain TRP-mimetic recognition motifs, thereby competing with endogenous TRP and interrupting the TRP-IDO1 metabolic cascade. To the best of our knowledge, there has been no report that endogenous tryptophan-derived nano-agents could simultaneously competitively inhibit IDO1 and activate the myelination pathway of SCs.

In this study, we demonstrate that TRP metabolism is commonly dysregulated in PNI, and the IDO1-driven KYN pathway is specifically activated. To target IDO1-regulated TRP metabolic reprogramming, for the first time, we developed a biomimetic tryptophan–Li^+ carbon dots (TLNDs) platform through the self-assembly of L-TRP and lithium carbonate (Li_2CO_3) via a mild, non-enzymatic catalytic oxidation and Schiff-base reaction, yielding ultrasmall nanoparticles with intrinsic fluorescence and superior aqueous solubility (at least 3 times that of L-TRP). The TLNDs inherited the

characteristic groups (e.g., indole rings, α-aminocarboxylic acid) in TRP, which could be specifically recognized by IDO1 and competitively bind to its active pocket, but did not participate in and affect the normal metabolism of TRP. Benefiting from this, the TLNDs exhibited a binding affinity for IDO1 that was significantly stronger than that of TRP (2.83-fold of K_D value calibrated by mass concentration). In addition, the introduction of Li^+ not only assisted the formation of TLNDs, but also had the ability to activate SCs autophagy as reported in our previous work [29], which could exert a synergistic effect with TRP metabolic regulation. Moreover, the TLNDs predominantly entered SCs via lipid raft-mediated endocytosis and displayed a remarkable preferential accumulation in lysosomes, where the dissociated Li^+ from TLNDs promoted lysosomal autophagy, thereby synergistically restored mitochondrial and lysosomal functions. Meanwhile, the TLNDs significantly enhanced lipophagy, reduced lipid droplets accumulation, facilitated cholesterol transport toward the cell membrane, and upregulated the expression of myelin-regeneration-associated proteins (Scheme 1). Through multi-omics profiling and IDO1 overexpression rescue experiments, we demonstrated that TLNDs effectively rewired TRP metabolism flux from the neurotoxic KYN pathway towards the neuroprotective 5-HT pathway. In a rat sciatic nerve crush model, subepineurial injection of TLNDs significantly suppressed neuroinflammation and ferroptosis, and promoted myelin repair and axonal regeneration. Since the dysregulation of the IDO1-KYN metabolic axis was also observed in diabetic peripheral neuropathy and neuropathic pain states, this novel IDO1 nano-inhibitor or similar IDO1-targeting strategies might have broad applicability across a spectrum of peripheral neurological diseases.



Scheme 1. Schematic illustration of the fabrication, targeted delivery, and therapeutic mechanism of TLNDs for peripheral nerve injury repair. Biomimetic tryptophan-Li^+ nanodots (TLNDs) were constructed for the first time by self-assembly of L-TRP and lithium carbonate through mild non-enzymatic catalytic oxidation and Schiff-base reaction. Owing to the preserved indole-ring structure, TLNDs competitively bind IDO1 with much higher affinity than free TRP. Predominantly internalized into Schwann cells via lipid raft-mediated endocytosis, TLNDs preferentially accumulate within lysosomes. Dissociated Li^+ from TLNDs activates lysosomal autophagy to synergistically rescue mitochondrial-lysosomal homeostasis. By mitigating oxidative stress and ferroptosis, TLNDs further relieve Schwann-cell apoptosis, enhance lipophagy, reduce lipid-droplet accumulation, facilitate cholesterol transport to the cell membrane, and elevate the levels of myelin-regeneration-associated proteins. Multi-omics profiling and IDO1 overexpression rescue experiments verify that TLNDs redirect TRP metabolic flux away from the neurotoxic KYN pathway toward the neuroprotective 5-HT pathway. Subepineurial delivery of TLNDs in rat sciatic-nerve-crush models represses neuroinflammation and ferroptosis, and improves myelin repair as well as axonal regeneration.

2. Results and discussion

2.1. Peripheral nerve injury induces dysregulation of TRP metabolism associated with Schwann cell IDO1

First, transcriptomic analysis uncovered 221 upregulated and 120 downregulated transcripts from an in vitro oxidative injury model developed by exposing rat primary Schwann cells (SCs) to TBHP (Fig. 1A and S1). Gene Ontology (GO) enrichment indicated a preponderance of terms related to cellular processes, e.g., metabolism signaling, membrane components, and catalytic/binding/transport molecular functions (Fig. 1B). Noteworthy, KEGG pathway mapping highlighted several notably altered pathways, including tryptophan metabolism, ferroptosis, GABAergic synapse, and cholesterol catabolism (Fig. 1C). The untargeted metabolomics corroborated that these transcriptional changes were accompanied by extensive metabolic rewiring. The principal component analysis distinctly separated the control and TBHP-treated groups (Fig. S2), and the volcano plot revealed numerous differential metabolites (Fig. S3), which belonged to 13 classes such as fatty acids, glycerolipids, and amino acid derivatives (Fig. S4). The KEGG analysis of these metabolites also revealed disruptions of fatty acid degradation, arachidonic acid metabolism and notably, tryptophan metabolism (Fig. S5). Combining the transcriptomic and metabolomic datasets, it concluded that TRP metabolic imbalance was one of the central correlates of oxidative dysfunctions in SCs (Fig. 1D), which was consistent with other nerve injuries [30].

Afterwards, TRP pathway metabolites were longitudinally measured in a rat sciatic nerve crush model to verify if this pattern of metabolism was replicated in vivo. As clearly shown in Fig. 1F, free TRP level dropped in the initial 3 days post-injury but rose again during 1-4 weeks. Conversely, KYN level and KYN/TRP ratio increased from the first day and peaked on day 3 (Fig. 1G-H). Besides, the neurotoxin QUIN peaked on day 7 (Fig. 1I), while the protective KYNA showed a gradual sustained increase till day 14 (Fig. 1J). In contrast to this, the levels of 5-HT decreased sharply at day 3 and subsequently started recovering (Fig. 1K). The above temporal dynamics establish that PNI induces overactivity in the IDO1–KYN axis that diverts TRP away from protective pathways and down toxic cascades that worsen tissue damage, a pattern

consistent with the observations of previous reported work [31]. Notably, the metabolic checkpoint function of IDO1 has been well documented in tumor immunity and in central neurodegenerative diseases such as Alzheimer's disease, Huntington's disease, and Parkinson's disease [32-34]. Current in vitro and in vivo results strongly suggest that this pathway is not simply passive and accidental, but rather an active driver of pathology. Therefore, it suggests that targeted intervention of excessive IDO1-TRP metabolic axis may constitute a novel and potential therapeutic route for PNI.

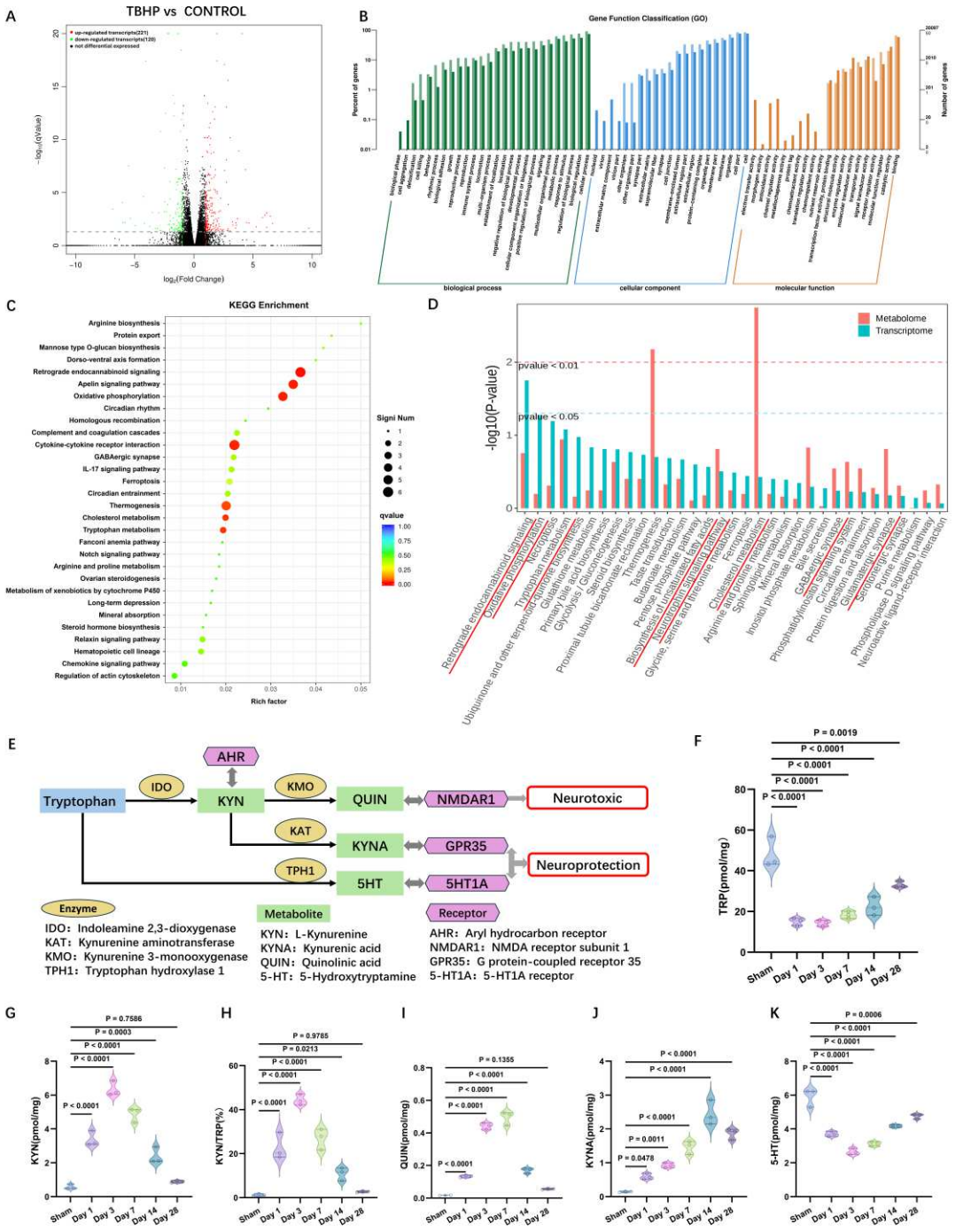


Fig. 1. Multi-omics profiling identifies TRP metabolism as a core pathological event in PNI. (A) Volcano plot showing differentially expressed genes (DEGs) between control and TBHP-treated Schwann cells. (B) Gene Ontology (GO) functional enrichment analysis of DEGs, categorized into biological process (BP), cellular component (CC), and molecular function (MF). (C) KEGG pathway enrichment analysis highlighting key altered pathways. (D) Integrated transcriptomic and metabolomic analysis showing the convergence of perturbed pathways. (E) Schematic illustration of the TRP metabolic pathway, depicting the neurotoxic (KYN/AHR, QUIN/NMDAR1) and neuroprotective (KYNA/GPR35, 5HT/5HT1A) branches. (F-K) Time-course changes of key TRP metabolites in rat sciatic nerve tissue following injury: (F) tryptophan (TRP), (G) kynurenine (KYN), (H) KYN/TRP ratio, (I) quinolinic acid (QUIN), (J) kynurenic acid (KYNA), and (K) 5-hydroxytryptamine (5-HT). Data are presented as mean ± SD. n = 3 per group.

2.2. Synthesis and physicochemical characterization of TLNDs

In view of the key pathogenic role of abnormal activation of the IDO1-KYN axis in SCs dysfunction, blocking IDO1 activity to restore the homeostasis of TRP metabolism and reduce the accumulation of neurotoxic metabolites represent a promising intervention strategy. Inspired by this, a TRP-derived biomimetic carbon dots (TNDs) exhibiting superior binding efficiency was developed to competitively occupy the catalytic pocket of IDO1. As shown in Fig. 2A, TNDs were synthesized based on non-enzymatic catalytic oxidation reaction. Mechanistically, L-tryptophan (TRP, **a1**) first dissolved with the assistance of carbonates (Li_2CO_3, Na_2CO_3, K_2CO_3) and forms tryptophan alkali metal salts (**a2**). The ionized carboxyl group and the deprotonated α-amino group increased the electron density of the indole ring in TRP, which drastically lowering the energy barrier for oxidative ring-opening. It was speculated that N-formylkynurenine (**b1**) and 2-amino-3-(2-oxoindolin-3yl) butanoic acid (**b2**) salts were two main products from indole oxidation of **a2** [35]. Afterwards, Schiff-base reaction between the aldehyde/lactamone and the amino groups continuously progressed, and nano-sized TNDs could be ultimately generated coupled with H-bonding interactions or conjugate stacking of indole rings (Fig. S6). We preliminarily screened TNDs synthesized from Li_2CO_3, Na_2CO_3, K_2CO_3 (namely TLNDs, TNNDs and TKNDs) and found that TLNDs could significantly promote the migration of RSC96 cells (Fig. S7), which was likely due to the activation of autophagy and cytoskeleton remodeling effects of Li^+ by inhibiting GSK3β pathway [36, 37]. Therefore, TLNDs were used as a representative for the following results discussion and subsequent applications. Benefiting from carboxyl ionization and nanocrystallization strategies, TLNDs possessed significantly higher water solubility than that of TRP, which could be increased by at least 3 times (Fig. S8). The above reaction hypothesis was preliminarily verified by morphological observation under Transmission Electron Microscopy (TEM). At the initial stage, lithium tryptophan showed typical appearance of salt crystals, while nanoparticles began to emerge with the extension of reaction time (Fig. 2B). The average particle sizes decreased from 31.74 nm at 1 h to 15.80 nm at 2 h, and ultimately yielding ultrasmall nanodots with a diameter of 3.21 nm (Fig. S9), which

might result from the subsequent oxidative etching and dehydrate fragmentation of large oligomeric clusters. Interestingly, the as-prepared TLNDs exhibited bright blue fluorescence under UV laser irradiation, and the intensity presented a gradually enhancing trend (Fig. 2B insets), which could be attributed to the C=N fluorophore from Schiff-base domains [38]. The photoluminescent spectra of TLNDs had an excitation-dependent characteristic, with the maximum excitation and emission wavelengths at 382 and 484 nm, respectively (Fig. S10).

It could be seen from the Fourier Transform Infrared (FT-IR) spectrum that most of the vibration peaks of TRP functional groups were retained in TLNDs, but the intensity ratios are different (Fig. S11). By normalizing the intensity of the indole aromatic C-H at 746 cm^{-1}, stronger signals at 1415 and 1456 cm^{-1} had arisen in TLNDs compared with TRP, possibly derived from the carboxyl groups generated by oxidation and indole ring-opening [39]. The characteristic band of Schiff-base ($\nu_{C=N}$) was coupled with the original COO^- vibration at 1593 cm^{-1}, thus the peak intensity was slightly increased in TLNDs after superposition. Then, ^{1}H-Nuclear Magnetic Resonance (NMR) spectroscopy was used to further analyze the possible changes of TLNDs. In the aromatic region (7-8 ppm), the peaks of TLNDs were similar to that of TRP, indicating that the structure of the benzene rings and the connected imine structures were basically retained (Fig. 2C). However, the ^{1}H signal of TLNDs in the aliphatic region (3-4 ppm) was uniformly downshifted by ~0.2 ppm, possibly due to the Li-ionization induction and long-range electron-withdrawing conjugation of carbonyl/C=N groups. The new peaks at 8.37 and 1.83 ppm of TLNDs originated from the imine proton (C=N) formed by Schiff-base condensation and saturated methine groups generated by the broken indole double bonds by ring-opening, respectively. Moreover, the proportion of O 1s peak of TLNDs markedly increased than that of TRP in X-ray Photoelectron Spectroscopy (XPS) detection, confirming that the catalytic oxidation reaction occurred (Fig. 2D). As expected, the singlet Li 1s peak existed in TLNDs with a binding energy of 55.3 eV, which was corresponded to the Li^+ state (Fig. 2E) [40]. Through element peak area fitting, the atomic percentage (At%) of Li^+ in TLNDs was calculated to be 7.8%, which was close to the mass fraction of 5.35% measured by Inductively Coupled

Plasma (ICP) (Fig. S12). Besides, the decrease of -NH_2 bonding ratio in N 1s and the increase of -OH in O 1s also proved the progression of Schiff-base reaction (Fig. S13).

In order to explore whether TLNDs could act as TRP analogues to compete for indoleamine 2,3-dioxygenase 1 (IDO1) binding, the direct interaction between TLNDs and IDO1 recombinant protein was verified by Surface Plasmon Resonance (SPR) experiments. The results showed that the binding strength (RU value) of TLNDs towards IDO1 revealed obvious concentration-dependent saturation binding characteristics (Fig. 2F). It was worth mentioning that the SPR test interval of TLNDs was set at mass concentration, due to the undefined molecular weight distribution of TLNDs. In the buffer elution stage, the slow dissociation of complexes confirmed the existence of dynamic and reversible molecular interactions between TLNDs and IDO1. The kinetic fitting revealed that the association rate constant (k_a) and dissociation rate constant (k_d) were 12.55 $(\mu g/mL)^{-1}s^{-1}$ and 1.22 s^{-1}, respectively, collectively verifying that TLNDs could directly and quickly bind IDO1. For TRP, the k_a and k_d values were 1.24×10^4 $M^{-1}s^{-1}$ (converted to mass concentration: 0.0607 $(\mu g/mL)^{-1}s^{-1}$) and 1.67×10^{-2} s^{-1}, respectively (Fig. S14), indicating that TLNDs possessed markedly faster association and dissociation rates than TRP. The kinetic equilibrium dissociation constant (K_D) calculated from the ratio of k_d to k_a was the core index representing the binding affinity. Notably, for ease of comparison, the K_D constant of TRP was converted to the same unit of TLNDs according to its relative molecular weight (0.275 μg/mL), which showed 2.83 times larger value than that of TLNDs (0.097 μg/mL), indicating a relatively higher affinity towards IDO1 of TLNDs. Although this comparison method was not very rigorous, the subsequent dose-effect curve of TLNDs inhibiting the activity of IDO1 and cellular thermal shift assay (CETSA) experiments could also prove that TLNDs indeed competed TRP binding IDO1 enzyme to block its KYN metabolism way. The SPR findings revealed that TLNDs and TRP displayed drastically divergent kinetic profiles, in other words, TLNDs underwent a more rapid association and dissociation processes relative to TRP, especially within the initial detection period. Despite the faster dissociation rate of TLNDs, its markedly elevated association rate ultimately yielded a lower K_D and stronger overall affinity, endowing it with prominent

competitiveness to occupy IDO1 binding pockets and block TRP recognition and subsequent metabolism. Although both TLNDs and TRP target the active site of IDO1, the unique molecular scaffold of TLNDs and the large specific surface area of nanodots may render the recognition mechanism, steric hindrance effect and conformational matching at the IDO1 binding pocket distinct from those of free TRP. The above high-precision kinetic measurements provide solid experimental evidence for further exploring TLNDs as a novel nanoinhibitor against IDO1.

Furthermore, Cellular Thermal Shift Assay (CETSA) analysis also validated the intracellular interaction between TLNDs and IDO1 (Fig. 2G). With the increase of temperature, the free IDO1 gradually unfolded and precipitated, the soluble protein in the supernatant decreased, and the gray scale of Western Blotting (WB) bands became lighter. However, the TLNDs group displayed deeper bands at the same temperature and the quantitative curve shifted to the higher temperature region (41-56°C) (Fig. S15), which proved that the IDO1 protein conformation was stable after the specific binding of TLNDs, that is, the TLNDs and IDO1 had direct interaction in cells. In order to explore the origin of stronger IDO1 binding ability of TLNDs than TRP, their combining energy barriers and interaction force types were theoretically simulated by molecular docking. As shown in Fig. 2H, we representatively simplified a dimer structure of TLNDs, and the calculated results demonstrated that the theoretical binding energy (BE) with IDO1 is -8.0 kcal/mol, apparently higher than -6.8 kcal/mol of TRP (Fig. S16). In particular, unlike the presence of only van der Waals and hydrogen bonding forces between tryptophan molecule and IDO1 receptor residues, TLNDs had more types of forces and active sites, such as hydrophobic interaction force, Pi-Pi stacked, amide-Pi stacked and Pi-alkyl forces (Fig. 2I). Combined with the high water dispersibility and large specific surface area of TLNDs, these characteristics together led to a better IDO1 competitive inhibition activity of TLNDs than TRP.

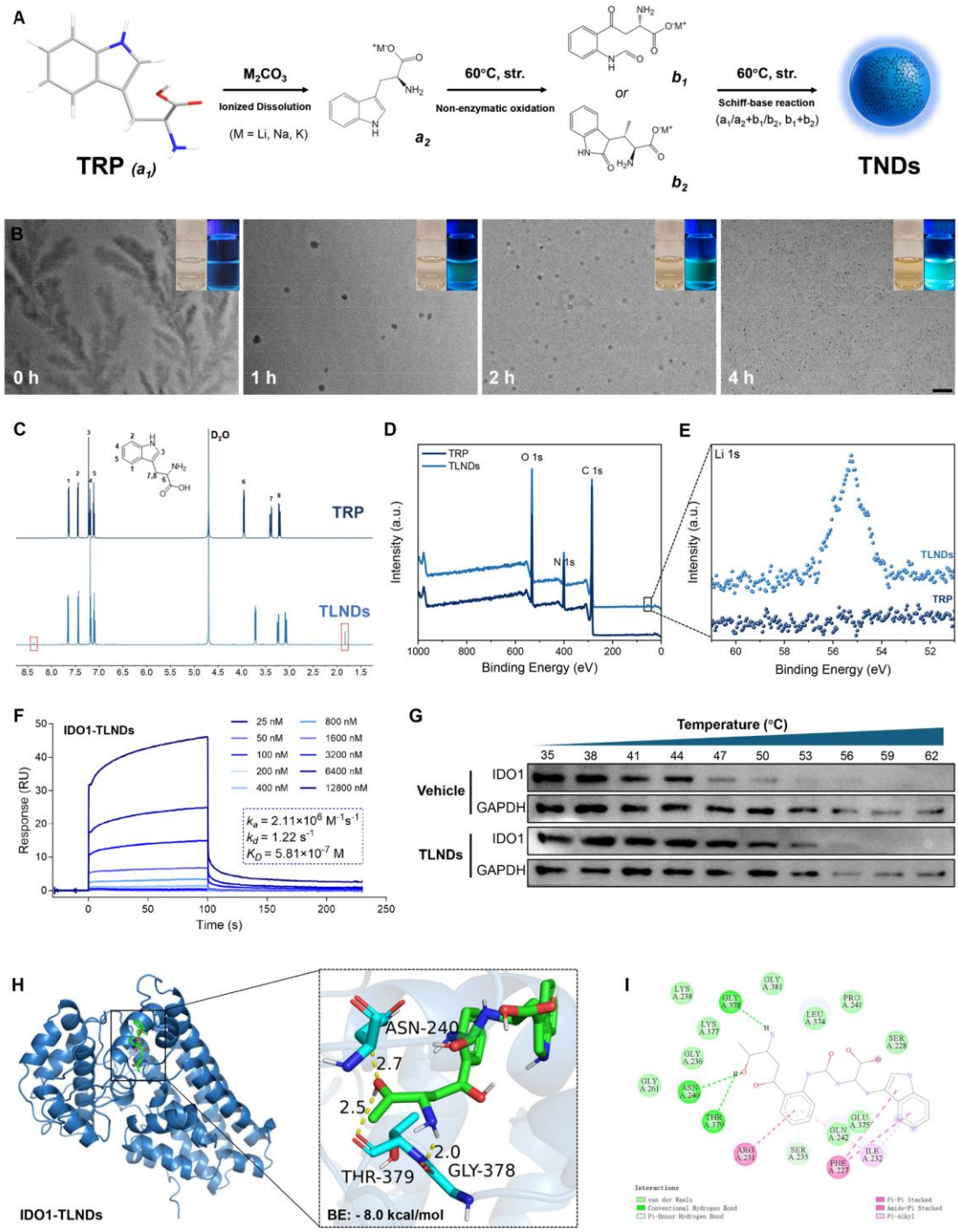


Fig. 2. TLNDs reaction process, structural characterization and IDO1 binding kinetics and theoretical simulation experiments. (A) Synthesis conditions and possible reaction mechanism of TNDs. (B) TEM images of TLNDs at different reaction times, photographs of TLNDs solutions under daylight and a hand-held UV light irradiation (scale bar = 100 nm). (C) 1H-NMR spectroscopy of TRP and TLNDs. (D) XPS full spectra and (E) Li 1s fine spectra of TRP and TLNDs. (F) SPR kinetic binding curve of TLNDs and IDO1 protein. (G) WB results of CETSA experiments of IDO1 and TLNDs at gradient temperatures (Vehicle: solvent control group). (H) Software visualized 3D binding mode diagram and (I) 2D action diagram of the interaction between TLNDs dimer model and IDO1 protein.

2.3. Biosafety, cellular uptake and subcellular localization of TLNDs

The biosafety profile of TLNDs was assessed before evaluating efficacy using CCK-8 assay, which showed that at doses even as high as 200 μg/mL, there was no cell death seen after 12 h of treatment (Fig. 3A). It was observed that the viability of TLNDs-treated cells was significantly higher than other groups from 12 h (Fig. 3B), indicating that TLNDs could promote the proliferation of RSC96 cells. The CCK-8 and AM/PI staining after exposure to TBHP further confirmed the protective effect of TLNDs, reflected in the stronger reduction degree of cell death than TRP monomer (Fig. 3G-I). Besides, the blood biochemical results of different concentrations and time gradients after continuous intraperitoneal injection of TLNDs in rats displayed that only the ALT level in the high-dose group increased transiently on 7 d, while other indicators such as AST, ALP and BUN were normal in each group (Fig. 3C-F). The histological examination of major organs also presented no evidence of tissue damage, inflammatory infiltration or necrosis (Fig. S17). The excellent biocompatibility of TLNDs can be attributed to endogenous TRP precursor, improved solubility and ultrasmall nanostructure, effectively circumventing the potential long-term toxicity concerns associated with synthetic inorganic or polymeric nanocarriers [41, 42].

Then, benefitting from the intrinsic fluorescence properties of TLNDs, we examined the ways how TLNDs enter SCs. By utilizing a panel of inhibitors, it was found that uptake was almost hindered upon use of 2-DG and lipid raft disruptor M-β-CD, while chlorpromazine had no effect, and amiloride/genistein only partially inhibited, indicating an energy-dependent uptake process via lipid raft-mediated endocytosis (Fig. 3J). This pathway that avoids the excessive inflammatory signaling often triggered by clathrin or caveolae-mediated uptake, thereby possibly favoring intracellular homeostasis [43]. Most of the internalized TLNDs were co-localized with lysosomal markers, with a small fraction dispersed in the cytoplasm (Fig. 3K). It had been confirmed that nanocarriers localized in lysosomes could efficiently regulate lysosome-related signaling pathways, thereby intervening in pathological processes, such as oxidative damage and apoptosis in cells [44]. It was speculated that the lysosomal localizability of TLNDs could be helpful to modulate lysosomal functions in lipid

handling and autophagic clearance [45], and the protonation of lithium carboxylate groups under lysosomal acidic conditions might also promote the responsive release of Li^+, thereby initiating a synergistic effect of metabolic regulation and autophagy activation.

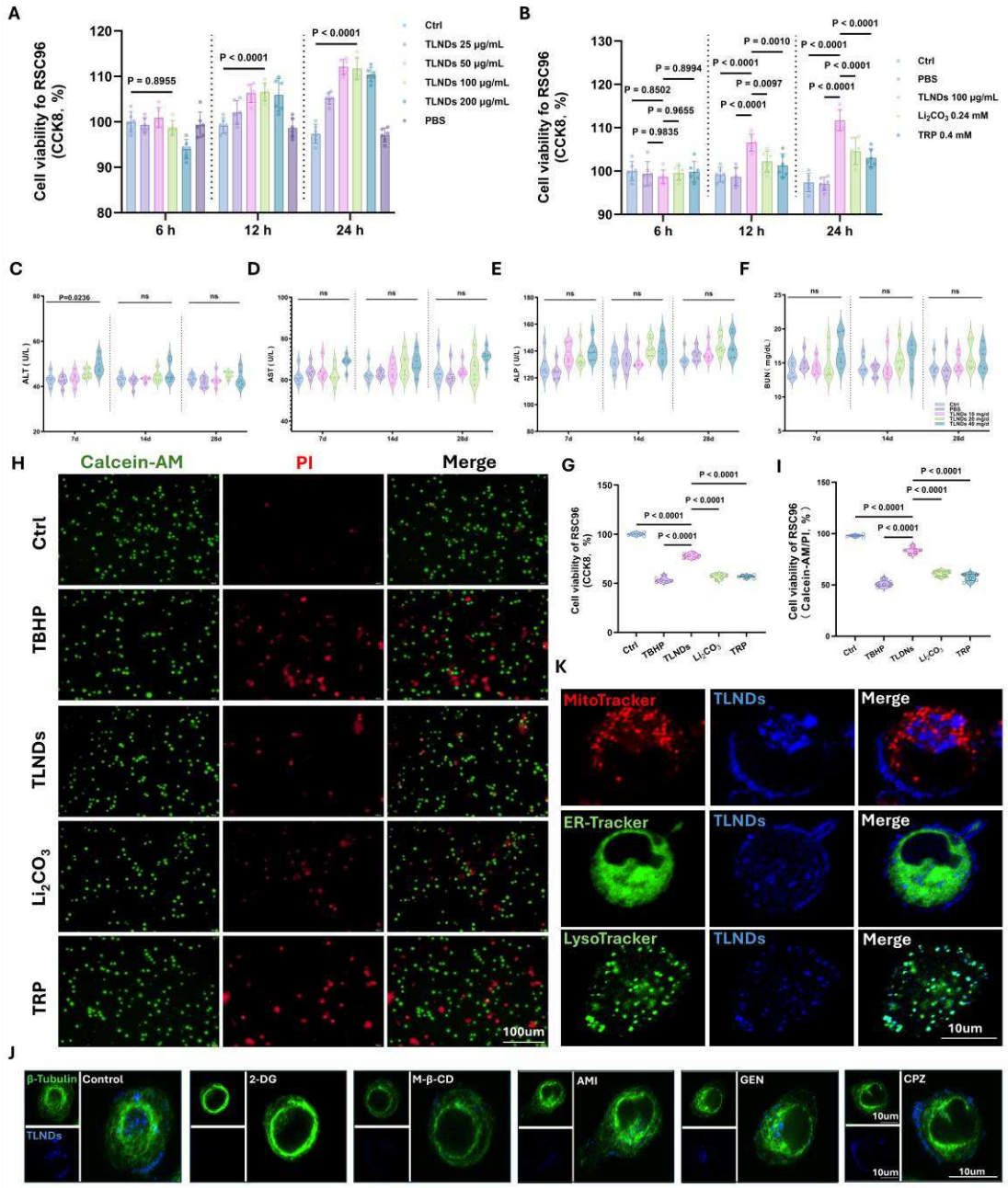


Fig. 3. Biosafety, cellular uptake, and cytoprotective effects of TLNDs in vitro. (A) Time-dependent cell viability of Schwann cells treated with increasing concentrations of TLNDs (25, 50, 100, 200 μg/mL) over 24 h assessed by CCK-8 assay. (B) Comparison of cell viability among TLNDs, free Li_2CO_3, free TRP, and control groups in Schwann cells. (C-F) In vivo biosafety evaluation: serum levels of (C) alanine aminotransferase (ALT), (D) aspartate aminotransferase (AST), (E) alkaline phosphatase (ALP), and (F) blood urea nitrogen (BUN) in rats treated with TLNDs. (G) CCK-8 assay demonstrating TLNDs-mediated protection against TBHP-induced

cytotoxicity. (H-I) Calcein-AM/PI live/dead staining: (H) representative fluorescence images (scale bar = 100 μm) and (I) quantification of the live/dead cell ratio. (J) Cellular uptake mechanism of TLNDs assessed using endocytosis inhibitors (2-DG, M-β-CD, AMI, GEN, CPZ; scale bar = 10 μm). (K) Subcellular localization of TLNDs co-stained with MitoTracker, ER-Tracker, and LysoTracker (scale bar = 10 μm). Data are presented as mean ± SD. n = 6 per group.

2.4. TLNDs remodel TRP metabolism and alleviate SCs inflammation in an IDO1-dependent manner

In order to carefully study the potential mechanism of TLNDs in improving the function of SCs, the phenotypic changes of SCs induced by TBHP before and after TLNDs treatment were analyzed by multi-omics. The PCA pattern showed obvious phenotypic segregation, and the related heat map revealed significant molecular remodeling affecting genes, proteins and metabolites (Fig. S18-19). Moreover, the KEGG enrichment identified oxidative phosphorylation, TRP metabolism, glutathione metabolism, and glycolysis/gluconeogenesis as significantly altered pathways (Fig. 4A). Interestingly, our metabolomics analysis of TLNDs on TRP pathway in nerve tissue and RSC96 cells revealed no alteration of IDO1 protein levels (Fig. 4E, S20, 4G). However, TLNDs led to a significant decrease in several toxic metabolites downstream of KYN, KYN/TRP ratio and QUIN, which corresponded to an increase in TRP itself and protective 5-HT (Fig. 4B-D, S21). As an endogenous ligand of AHR [46], the decrease of KYN may alleviate the inhibition of AHR-mediated axon regeneration (Fig. 4G, S20). To clarify whether IDO1 acts as a critical upstream regulatory mediator, an overexpressed IDO1 model in RSC96 was established via lentiviral transduction, which confirmed that TLNDs exerted protective effects on SCs by inhibiting IDO1 activity (Fig. 4F). TLNDs had contrasting impacts on two different gene sets in addition to metabolic changes, including the inhibition of AHR, KMO and NMDAR1 associated with excitatory toxicity and pro-inflammatory signaling, as well as upregulation of TPH1, 5HT1A, KAT2 and GPR35, which are conducive to 5-HT synthesis and neuroprotection (Fig. 4G, S22). Such coordinated changes indicated that TLNDs did not negatively regulate IDO1 expression but rather block its enzymatic action. As mentioned before, IDO1 is a key rate-limiting enzyme in TRP metabolism, and the abnormal activation of the KYN pathway driven by IDO1 is related to the pathogenesis

of various neurological diseases [47]. In this study, this mechanistic paradigm was extended to PNI, and new intervention strategies were designed. The TLNDs-mediated IDO1 inhibition reduced the level of neurotoxic QUIN and increased the level of neuroprotective 5-HT without disturbing the expression of IDO1 protein (Fig. 4H).

To investigate if TLNDs directly inhibit the catalytic activity of IDO1, an in vitro enzymatic assay was conducted with cell-free recombinant human IDO1 protein. As highlighted in Figure S23, there was a concentration-dependent inhibition of the IDO1-mediated conversion of TRP to KYN by TLNDs. The IC_{50} value was 9.776 μg/mL (95%, CI: 8.89-10.81 μg/mL), with a 0.907 hillslope of the dose-response curve. The observed results indicated the capacity of TLNDs to bind and directly inhibit the enzymatic activity of IDO1 independent of protein level, which was in line with the increased thermal stability of IDO1 upon TLNDs binding observed in the CETSA assay. In addition to metabolic and oxidative disturbances, sustained neuroinflammation is the major determinants of PNI outcome. Indeed, the release of TNF-α, IL-1β, IL-6 and NF-κB phosphorylation were significantly raised by TBHP simulation in SCs cultures (Fig. 4I, S24). As expected, TLNDs treatment simultaneously suppressed NF-κB signaling activation and pro-inflammatory cytokine secretion, and these effects could be eliminated by IDO1 overexpression (Fig. 4I, S24). Furthermore, the histological analysis of the crushed sciatic nerve tissues confirmed the above findings, which showed a dense inflammatory infiltrate in the injury area while the TLNDs group exhibited obvious reduction of inflammatory and neutrophil invasion (Fig. 4J-K).

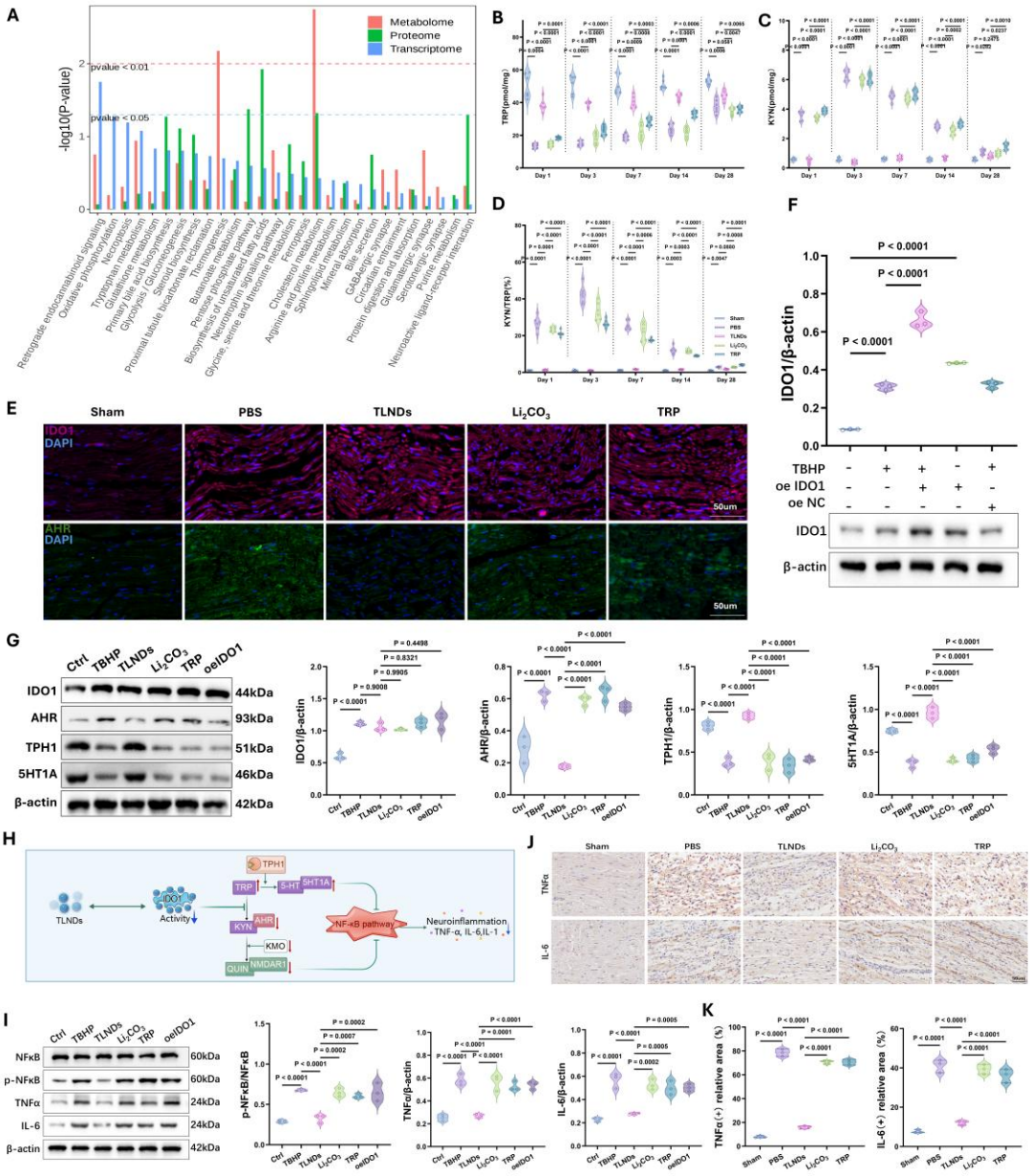


Fig. 4. TLNDs remodel TRP metabolism and alleviate Schwann cell inflammation in an IDO1-dependent manner (A) KEGG enrichment analysis based on integrated multi-omics data. (B-D) Quantification of core TRP metabolites in PNI nerve tissues: (B) TRP, (C) KYN, and (D) KYN/TRP ratio. (E) Representative immunofluorescence staining of sciatic nerve sections for IDO1 and AHR (scale bar = 50 μm). (F) Validation of IDO1 overexpression in RSC96 cells via lentiviral transduction. (G) Western blot and quantitative analysis of key enzymes (IDO1, TPH1) and receptors (AHR, 5HT1A) in the TRP pathway in RSC96 cells. (H) Schematic diagram showing that TLNDs regulate TRP metabolic reprogramming, inhibit NF-κB signaling and alleviate neuroinflammation. (I) Western blot and quantitative analysis of inflammatory signaling proteins (NF-κB, p-NF-κB, TNF-α, IL-6) in RSC96 cells under different treatments. (J) Immunohistochemical staining of nerve tissue for TNF-α and IL-6 (scale bar = 50 μm). (K) Quantification of TNF-α and IL-6 staining intensity. Data are presented as mean ± SD. n = 6 per group for (A-D); n = 3 per group for (E-K).

2.5. TLNDs restore mitochondrial redox homeostasis, alleviate ferroptosis and apoptosis

As mentioned before, IDO1-mediated TRP metabolism disorder is closely linked to mitochondrial dysfunction and the ferroptosis process, representing a key pathological regulatory node in PNI [48]. In RSC96 cells, TBHP provoked total and mitochondrial ROS (Fig. 5A-D), collapsed mitochondrial membrane potential (Fig. 5E-F), and depleted ATP production (Fig. 5J), all of which were effectively reversed by the addition of TLNDs. Similarly, the intervention outcomes of TLNDs disappeared in the IDO1 protein overexpressed cells, which strongly supported the view that IDO1 was the key mediator in the enhancement of mitochondrial function by TLNDs. Moreover, the same dependency was also observed for ferroptosis-related markers, i.e., NRF2-HO1 axis (Fig. S25), SOD, GSH, and MDA level (Fig. 5G-I), ACSL4, SLC7A11, GPX4, and Ferritin expression (Fig. 5M), as well as free iron accumulation (Fig. 5K-L). Also, oxidative damage increased the expression ratio of BAX/BCL-2 in SCs and triggered the cleavage of Caspase-3, both of which were markers of apoptosis, whereas TLNDs significantly altered these changes (Fig. 5N). The same conclusion was also confirmed by immunofluorescence staining of BAX and BCL2 in the sciatic nerve of PNI rats (Fig. 5O). TLNDs reduce cellular and mitochondrial ROS accumulation, alleviate oxidative stress damage and ferroptosis, inhibit cell apoptosis, and restore the homeostasis of Schwann cells (Fig. 5P).

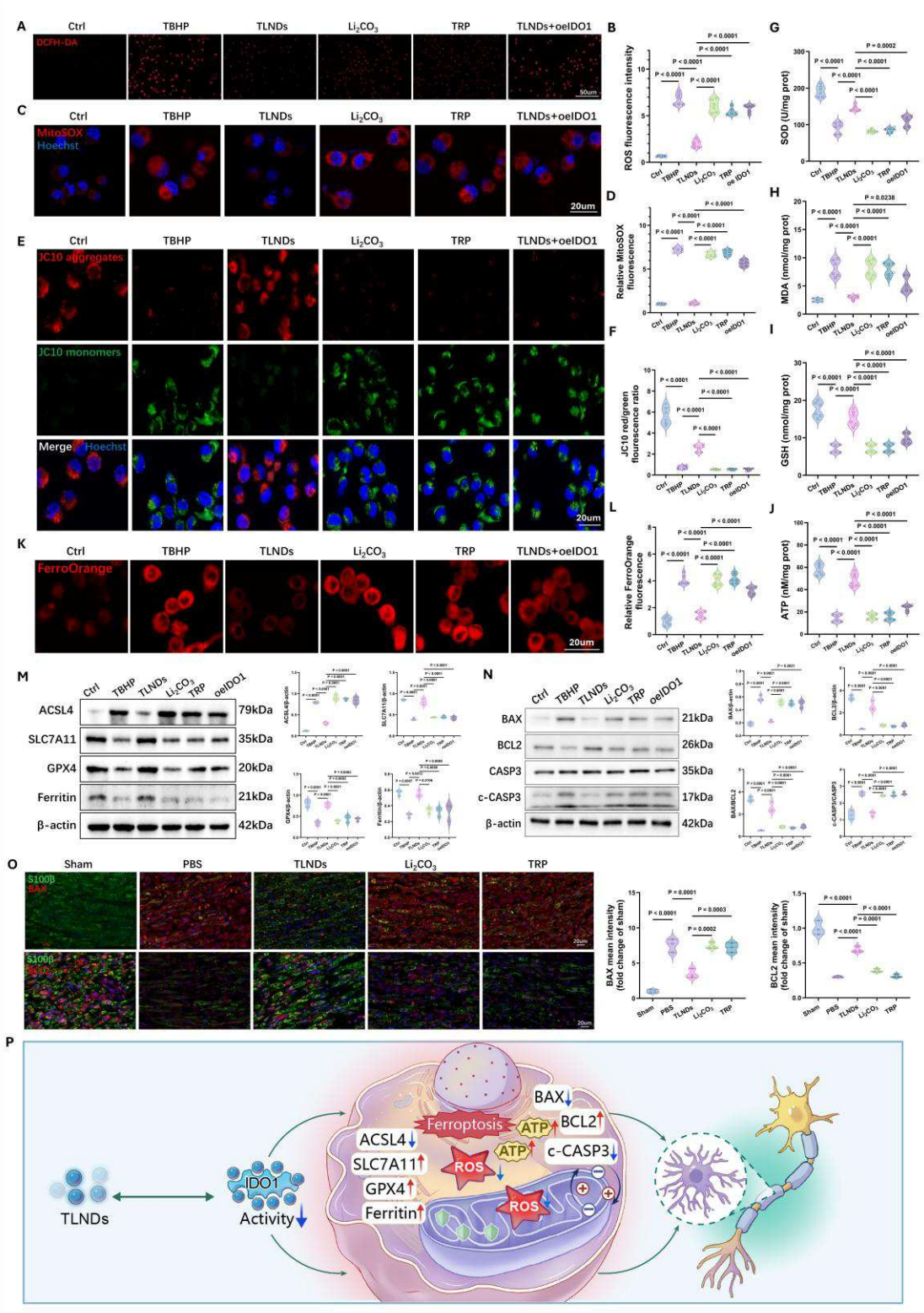


Fig. 5. TLNDs restore mitochondrial redox homeostasis and alleviate ferroptosis and apoptosis. (A-B) Representative fluorescence images and quantification of intracellular reactive oxygen species (ROS) using DCFH-DA staining (scale bar = 50 μm). (C-D) Representative fluorescence images and quantification of mitochondrial ROS using MitoSOX staining (scale bar = 20 μm). (E-F) JC-10 staining for mitochondrial membrane potential (ΔΨm): (E) representative images (scale bar = 20 μm) and (F) quantification of the red/green fluorescence ratio. (G-J) Quantification of (G) superoxide dismutase (SOD) activity, (H) malondialdehyde (MDA) levels, (I) reduced glutathione

(GSH) levels, and (J) ATP levels. (K-L) Representative fluorescence images and quantification of intracellular Fe^{2+} using FerroOrange staining (scale bar = 20 μm). (M) Western blot and quantitative analysis of ferroptosis-related proteins (ACSL4, SLC7A11, GPX4, Ferritin). (N) Western blot and quantitative analysis of apoptosis-related proteins (BAX, BCL2 CASP3, c-CASP3). (O) Representative immunofluorescence staining and quantification of sciatic nerve sections for BAX and BCL2 (scale bar = 20 μm). (P) Schematic diagram of TLNDs in reducing cellular and mitochondrial ROS, alleviating oxidative-stress injury and ferroptosis, inhibiting apoptosis, and restoring Schwann cell homeostasis. Data are presented as mean ± SD. n = 6 per group for (A-L); n = 3 per group for (M-O).

2.6. TLNDs restore lysosomal function and lipophagy in SCs and modulate cholesterol transport to facilitate myelin repair

Lipophagy, an important type of selective autophagy, primarily relies on lysosomes to degrade intracellular lipid droplets and is a key biological process for maintaining SCs homeostasis. After PNI, a plenty of disintegrated myelin fragments usually cause abnormal accumulation of lipids in SCs and lysosomal structural damage, which hinder lipid phagocytosis pathway for debris removal [49]. First, the effects of oxidative damage and TLNDs on the structure and function of lysosomes were explored. Lysosomal membrane protein LAMP1 is a classic marker of lysosomal integrity, and cathepsin B (CTSB) is a key hydrolase in lysosomes. The expression levels of both directly reflect the structural integrity and degradation ability of lysosomes [50]. Besides, Transcription factor EB (TFEB), as a core molecule regulating lysosomal biogenesis and functional activation, determines the overall transcriptional efficiency of lysosome-related genes through its nuclear translocation level [51]. It had shown that TBHP inhibited LysoTracker staining and downregulated CTSB and LAMP1 (Fig. 6A-E, S26), indicating the damage of lysosomal structure and functions. All these parameters were restored by TLNDs, and importantly, they promoted the nuclear translocation of TFEB (Fig. 6C), which were the major transcriptional regulators of lysosomal biosynthesis. This result indicated that TLNDs did not simply repair damaged lysosomes, they also promoted lysosome supplementation by activating biosynthesis-related transcription.

To further focus on lipophagy pathway, a form of lipid droplet degradation that occurs in lysosomes, the co-localization of lipid metabolism-related protein expression in lysosomes was studied in detail. As shown in Fig. 6F-G, the lipid droplet

accumulation and increased expression of PLIN2 were observed in damaged SCs, along with the disrupted autophagic flux that was indicated by the increased level of LC3 and P62. Noteworthy, the induction of TLNDs not only improved the abnormal lipid metabolism, but also enhanced the physical contact between lysosomes and lipid droplets (Fig. 6F). As we have seen throughout the study, due to the overexpression of IDO1, the intervention effects of TLNDs were all negated, confirming that lipophagy is also IDO1-dependent. Cholesterol, as the main lipid component of myelin sheath, its synthesis, transport and distribution directly determine the structural integrity and physiological function of peripheral nerve myelin sheath [52]. Using NBD-cholesterol labeling, it was intuitively found that TBHP significantly affected cholesterol distribution because it tended to dispersed in the cytoplasm rather than in the plasma membrane (Fig. 6H-I). After TLNDs intervention, the total free cholesterol content in the cells was significantly reduced (Fig. 6L), and the directional transport efficiency to the cell membrane was significantly improved, and the co-localization level of cholesterol and cell membrane was also basically restored (Fig. 6J-K). At the molecular level, NPC1, NPC2 and ABCG1 in SCs, including lysosomal cholesterol export and efflux transporters, were down-regulated after oxidative damage. Among them, NPC1 and NPC2 are core cholesterol transporters located in lysosomes, which synergistically transport cholesterol from lysosomes to cytoplasm and other organelles, while ABCG1 is an important membrane transporter that mediates cholesterol outward transport to maintain cellular lipid balance [53]. The TLNDs re-established the transport pathway of these three types of abnormally expressed proteins, which could directly lead to the effective improvement of cholesterol transport and accumulation (Fig. 6M-N). Further, IDO1 overexpression again offsets the up-regulation of TLNDs, demonstrating that this effect is achieved by targeting the IDO1-TRP metabolic axis. Finally, the expression levels of myelin-associated proteins, including MBP, PLP, and MAG were evaluated to represent the structural integrity and regeneration ability of myelin sheath [54]. It also showed that TLNDs obviously restored the decreased expression of myelin protein, but failed in IDO1-overexpressed cells (Fig. 6O-P), further confirming that TLNDs stimulated myelin regeneration through cholesterol homeostasis recovery in an IDO1-

dependent manner. Collectively, TLNDs restored lysosomal function, enhanced lipophagy, reduced lipid droplet accumulation, promoted cholesterol transport to the cell membrane, and facilitated myelin regeneration (Fig. 6Q).

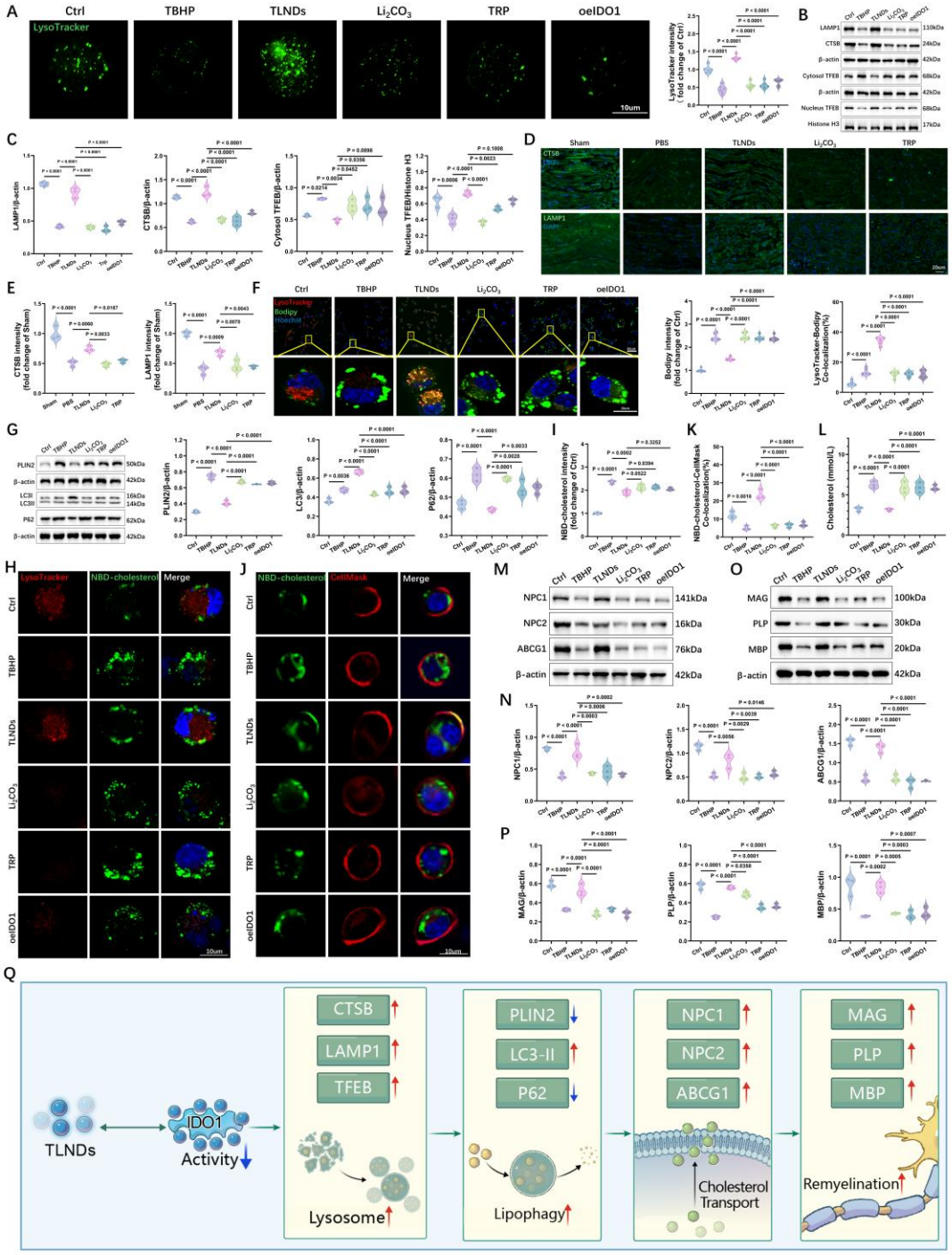


Fig. 6. TLNDs restore lysosomal function and lipophagy in Schwann cells and modulate cholesterol transport to facilitate myelin repair. (A) Representative LysoTracker staining and quantification of lysosomes in different treatment groups (scale bar = 10 μm). (B) Western blot analysis of lysosomal markers (LAMP1, CTSB) and TFEB in cytosolic and nuclear fractions. (C) Quantification of LAMP1, CTSB, cytosolic TFEB, and nuclear TFEB. (D) Immunofluorescence

staining of sciatic nerve tissue for LAMP1 and CTSB (scale bar = 20 μm). (E) Quantification of CTSB and LAMP1 fluorescence intensity in nerve tissue. (F) Co-staining of BODIPY (lipid droplets) and LysoTracker to assess lipophagy (scale bar = 10 μm). Quantification of BODIPY intensity and LysoTracker-BODIPY colocalization rate. (G) Western blot and quantitative analysis of lipophagy-related proteins (PLIN2, LC3, P62). (H) Co-staining of LysoTracker and NBD-cholesterol in RSC96 cells (scale bar = 10 μm). (I) Quantification of intracellular NBD-cholesterol fluorescence intensity. (J) Co-staining of NBD-cholesterol and CellMask plasma membrane stain (scale bar = 10 μm). (K) Quantification of plasma membrane-localized cholesterol. (L) Total cholesterol content measured by biochemical assay. (M) Western blot analysis of cholesterol transporters (NPC1, NPC2, ABCG1). (N) Quantification of NPC1, NPC2, and ABCG1. (O) Western blot analysis of myelin-related proteins (MAG, PLP, MBP). (P) Quantification of MAG, PLP, and MBP. (Q) Schematic diagram depicting that TLNDs restore lysosomal function, boost lipophagy, mitigate lipid-droplet accumulation, facilitate cholesterol transport toward the cell membrane, and promote myelin regeneration. Data are presented as mean ± SD. n = 6 per group for (A, F); n = 3 per group for (B-E, G-P).

2.7. TLNDs improve motor function and neural morphology after injury

Subsequently, to verify whether TLNDs can promote peripheral nerve regeneration in vivo by remodeling the TRP-IDO1 metabolic axis, a rat sciatic nerve crush injury model was constructed and TLNDs were microinjected under the epineurium after injury. There was no difference in the sciatic nerve function index (SFI) between the two groups on the 7th day, because early injury recovery had not yet been reflected in the rat foot gait. However, on day 14 and 28, the SFI value of TLNDs group was significantly better than the PBS, free TRP or Li_2CO_3 groups (Fig. 7B), which was also proved by the electrophysiological activity record. The hind limbs of rats treated with TLNDs showed larger compound muscle action potential (CMAP) amplitude, showing shorter latency and faster conduction velocity (Fig. 7C). After peripheral nerve crush injury, nerve impulse conduction is interrupted and nutrient supply is unbalanced, which can induce disuse atrophy and tissue fibrosis of distal target muscles. Therefore, the morphological changes of the target muscle are also important indicators for evaluating the effectiveness of nerve repair [55]. Compared with the injury group, the wet weight of the triceps surae muscle and the cross-sectional area of the muscle fibers increased and the fibrosis deposition decreased in the TLNDs group at 28 d (Fig. 7D, 7F and S27). Moreover, Toluidine blue staining and high-resolution transmission electron microscopy (TEM) images of the distal nerve at the injury site revealed significant differences (Fig. 7E). The nerve fibers in the PBS and TRP treatment group

were sparse and disordered, and the myelin sheath was loose and degraded. However, in the TLNDs group, the fibers were arranged neatly, the sheath was thick and complete, and the axon contour was healthier. Also, the quantitative statistical results demonstrated that TLNDs increased the number of myelinated nerve fibers, increased the diameter of axons, and normalized the G-ratio (Fig. 7G-I). What's more, immunofluorescence of sciatic nerve sections on day 28 showed that MBP and neurofilament heavy chain (NF-H) signals were significantly enhanced in the TLNDs group (Fig. 7J-K), which were markers of myelin integrity and axonal cytoskeleton, respectively [56]. Their synchronous up-regulation after the treatment of TLNDs indicated that not only the number of regenerated axons increased, but also mature myelination support was obtained. In order to complement tissue observation, PC12 cells and dorsal root ganglion (DRG) explant cultures were further introduced as these are effective and intuitive systems for evaluating neurite outgrowth. The synaptic length of PC12 cells in the TLNDs group was approximately 5-fold higher than that in the other groups (Fig. 7L-M). β-Tubulin staining showed that compared with the control group and the monomer group, the explants of the TLNDs treatment group showed longer neurites and greater axon density (Fig. 7N-O). The consistency of the two independent models proves that TLNDs have the activity of promoting axon growth and may contribute to the recovery of function in vivo.

Based on the above results, the functional reconstruction of TLNDs on injured sciatic nerves can be understood by the synergistic effect of its two active components, that is, 1) TLNDs have biomimetic TRP nanostructures, competitively inhibit IDO1, block the harmful shunt of TRP to KYN pathway, which reduce the accumulation of neurotoxic metabolite QUIN and increase the level of neuroprotective metabolite 5-HT, thereby establishing a metabolically allowable microenvironment for the survival and differentiation of SCs [57, 58]; 2) Li^+ released from TLNDs can directly drive the transcription of key myelin genes such as MPZ and the activation of autophagy pathway, and assist in improving the lysosomal and mitochondrial functions of SCs [36, 59]. Collectively, we herein developed a synergistic therapeutic strategy integrating TRP metabolic pathway remodeling and SCs functional activation for efficient PNI repair.

This cooperative strategy provides a new insight into the design of IDO1 selective nano-inhibitors, which are used to correct the deviated enzyme metabolic pathway after injury, thereby providing a good regenerative microenvironment for nerve regeneration.

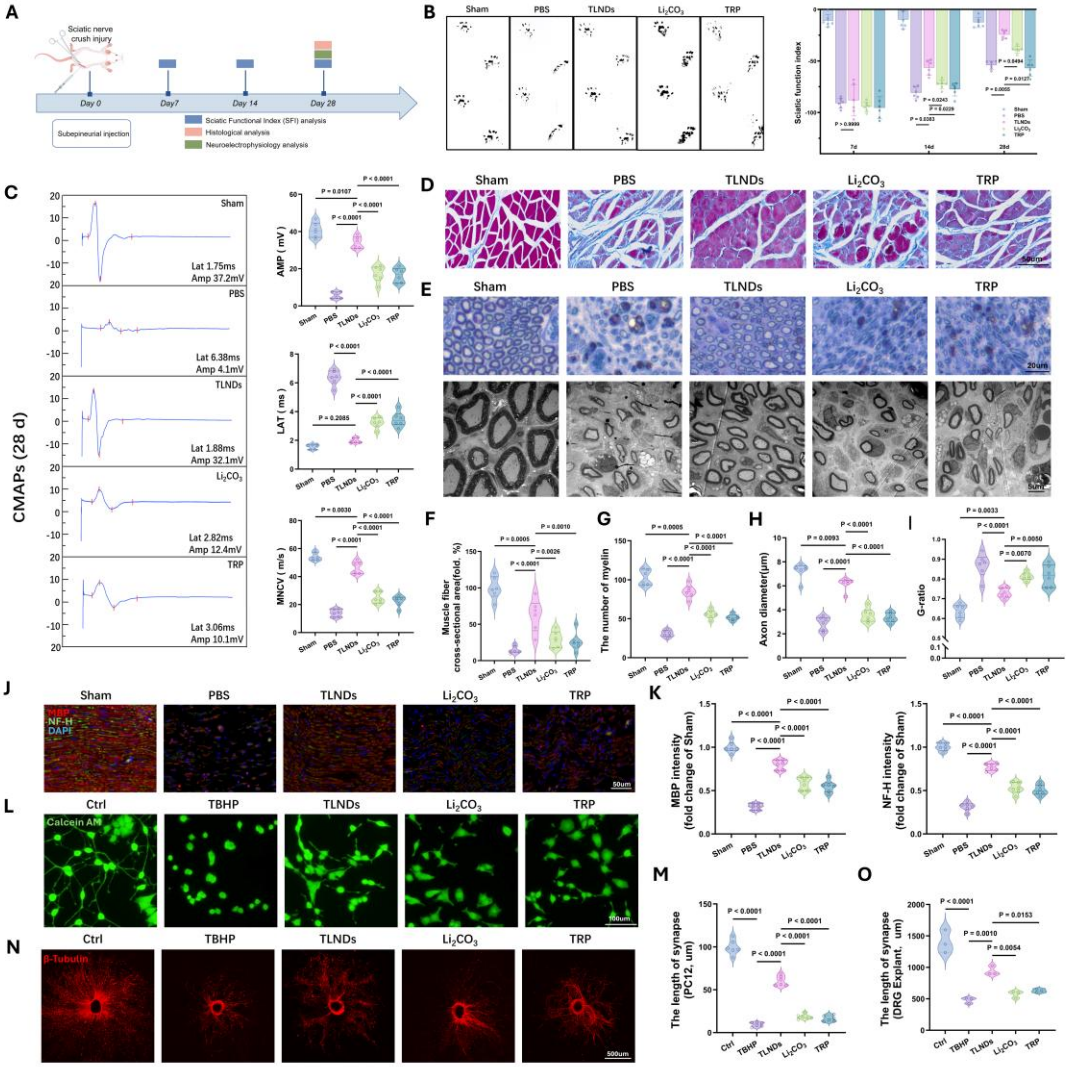


Fig. 7. TLNDs boost peripheral nerve axonal regeneration, remyelination and functional recovery. (A) Schematic illustration of the in vivo experimental design and treatment timeline. (B) Sciatic functional index (SFI) assessed at 7-, 14-, and 28-days post-injury. (C) Electrophysiological assessment at day 28: representative compound muscle action potential (CMAP) traces, CMAP amplitude (AMP), latency (LAT), and motor nerve conduction velocity (MNCV). (D) Representative Masson's trichrome staining of gastrocnemius muscle sections (scale bar = 50 μm). (E) Representative toluidine blue staining of regenerated nerve fibers (scale bar = 20 μm) and transmission electron microscopy (TEM) images of myelin sheaths (scale bar = 5 μm). (F) Quantification of muscle fiber cross-sectional area. (G-I) Quantification of (G) the number of myelinated fibers, (H) axon diameter, and (I) G-ratio. (J) Representative immunofluorescence staining of sciatic nerve sections for neurofilament heavy chain (NF-H) and myelin basic protein (MBP; scale bar = 50 μm). (K) Quantification of MBP and NF-H fluorescence intensity. (L) Representative images of differentiated PC12 cells under different treatments (scale bar = 100 μm). (M) Quantification of neurite length in PC12 cells. (N) Representative images of dorsal root

ganglion (DRG) explant cultures stained with β-Tubulin (scale bar = 500 μm). (O) Quantification of neurite length in DRG explants. Data are presented as mean ± SD. n = 6 per group for (A-M); n = 3 per group for (N-O).

3. Materials and methods

3.1. Materials

L-tryptophan, lithium carbonate (Li_2CO_3), sodium carbonate (Na_2CO_3), potassium carbonate (K_2CO_3), 1-ethyl-3-(3-dimethylaminopropyl) carbodiimide (EDC), N-hydroxysuccinimide (NHS) were purchased from Aladdin (Shanghai, China). Rat RSC96 Schwann cells were procured from the Cell Bank of the Chinese Academy of Sciences (Shanghai, China). Dulbecco's modified Eagle's medium (DMEM, high glucose), fetal bovine serum (FBS), penicillin–streptomycin, and trypsin were supplied by Gibco (Thermo Fisher Scientific, Shanghai, China). Collagenase I, forskolin, neuregulin-1 beta (NRG1-β1), cytosine arabinoside (Ara-C), puromycin, poly-L-lysine, and tert-butyl hydroperoxide (TBHP) solution were purchased from Shanghai Macklin Biochemical Co., Ltd. (Shanghai, China). The Cell Counting Kit-8 (CCK-8), Calcein-AM/PI live/dead staining kit, Mito-Tracker, Lyso-Tracker, ER-Tracker, CellMask plasma membrane stain, DCFH-DA, MitoSOX Red, JC-10, BODIPY 493/503, NBD-cholesterol, and ferrous ion probe were obtained from Beyotime Biotechnology (Shanghai, China). Endocytosis inhibitors, including 2-deoxy-D-glucose (2-DG), methyl-β-cyclodextrin (M-β-CD), amiloride (AMI), genistein (GEN), and chlorpromazine (CPZ), were sourced from MedChemExpress (Shanghai, China). Commercial kits for superoxide dismutase (SOD), malondialdehyde (MDA), reduced glutathione (GSH), adenosine triphosphate (ATP), aspartate aminotransferase (AST), alanine aminotransferase (ALT), alkaline phosphatase (ALP), and blood urea nitrogen (BUN) were bought from Nanjing Jiancheng Bioengineering Institute (Nanjing, China). Enzyme-linked immunosorbent assay (ELISA) kits for tumor necrosis factor-α (TNF-α), interleukin-1β (IL-1β), interleukin-6 (IL-6), and cathepsin B (CTSB) came from the same supplier. RIPA lysis buffer, protease and phosphatase inhibitor cocktail, enhanced chemiluminescence (ECL) substrate, and DAPI were acquired from Beyotime Biotechnology (Shanghai, China). Polyvinylidene

difluoride (PVDF) membranes and precast 10% SDS-PAGE gels were obtained from Shanghai Epizyme Biomedical Technology Co., Ltd. (Shanghai, China). Matrigel basement membrane matrix was purchased from Corning (Shanghai, China). Triton X-100, phosphate-buffered saline (PBS), and other analytical-grade reagents were obtained from Sinopharm Chemical Reagent Co., Ltd. (Shanghai, China) unless otherwise noted.

3.2. Synthesis and characterization of TNDs

L-tryptophan (204.2 mg, 1 mmol) and Li_2CO_3 (44.3 mg, 0.6 mmol) were mixed and ultrasonically dispersed in a glass scintillation bottle containing 10 mL DI water, stirred and placed in a 60°C water bath for further dissolution, and then heated for 4 h. The solution was passed through a 0.22 μm polyethersulfone filter to remove insoluble salts, and dialyzed with a CE membrane with a molecular weight cut-off of 1000 Da for at least 48 h until the inner solution was neutral. Finally, the product was collected and freeze-dried to obtain tryptophan-Li^+ carbon dots (TLNDs) powder. For the synthesis of tryptophan-Na carbon dots (TNNDs) and tryptophan-K carbon dots (TKNDs), the synthesis and post-treatment procedures were the same as above, except that Li_2CO_3 was replaced by Na_2CO_3 and K_2CO_3, respectively.

Transmission Electron Microscopy (TEM) images were photographed on JEM-2100F (JEOL, Tokyo, Japan). Photoluminescence (PL) and Ultraviolet-visible (UV-vis) absorption spectra were measured on RF-5301PC and UV-3100 spectrophotometer (Shimadzu, Kyoto, Japan), respectively. Fourier Transform Infrared (FT-IR) spectra were recorded on Nicolet Avatar 360 FTIR spectrometer (Thermo Fisher Scientific, MA, USA). 1H-Nuclear Magnetic Resonance (NMR) spectra were conducted on AVANCE III 600 MHz (Bruker, Ettlingen, Germany). X-ray Photoelectron Spectroscopy (XPS) was performed on ESCALAB 250 spectrometer (Thermo Fisher Scientific, MA, USA) equipped with a monochromatic Al Kα X-ray source (1486.6 eV). The Li content was tested by Agilent 725 inductively coupled plasma spectrometer (ICP) (Agilent Technologies, CA, USA).

3.3. Primary and Schwann cells culture

Sciatic nerves dissected from 3 day-old Sprague-Dawley rats were freed of epineurium, minced, and digested using 0.1% collagenase I and 0.125% trypsin at 37°C for 45 min. The resulting suspension was filtered, centrifuged, and plated on poly-L-lysine-coated dishes in high-glucose DMEM supplemented with 10% FBS, forskolin, and NRG1-β1. Fibroblast contamination was eliminated by treatment with Ara-C for 72 h, followed by differential adhesion purification. Cells at passages 2-3 exhibited >95% purity as verified by S100β/P75NTR immunofluorescence. RSC96 cells were maintained in high-glucose DMEM containing 10% FBS and 1% penicillin-streptomycin at 37°C in a 5% CO_2 atmosphere [60, 61].

3.4. TBHP-induced oxidative damage model in Schwann cells

Primary rat Schwann cells were exposed to TBHP at concentrations of 25, 50, 100, 200, or 400 μM for 4 h. CCK-8 assays indicated that 100 μM TBHP reduced viability to approximately 50%, which was chosen as the optimal modeling condition. All drug pretreatments were administered 4 h prior to TBHP challenge.

3.5. Multi-omics detection and integrated analysis

Primary rat Schwann cells from control, TBHP-injured, and TLNDs-pretreated + TBHP groups were sent for multi-omics profiling (Shanghai Sangon Biotech Co., Ltd.). Total RNA was isolated with TRIzol, checked for quality, and sequenced on an Illumina NovaSeq 6000 platform. Differentially expressed genes (DEGs) were identified using DESeq2. Proteins were extracted with RIPA buffer and analyzed by Easy-nLC 1200-Q Exactive HF-X mass spectrometry. Differentially expressed proteins (DEPs) were annotated with MaxQuant against the UniProt rat database. Metabolites were extracted with a methanol/acetonitrile/water mixture and subjected to UHPLC-Q-Exactive analysis to define differentially expressed metabolites (DEMs). All DEGs, DEPs, and DEMs were mapped to KEGG pathways for enrichment. Pearson correlation analyses among key molecules were used to construct regulatory networks, thereby clarifying oxidative damage and antioxidant responses in primary Schwann cells.

3.6. Molecular docking theoretical simulation

The 2D structure of the small molecule ligand was obtained from the PubChem database and imported into Chem3D 23.1.1 software to construct and optimize the 3D structure, which was saved as a mol2 format file. The crystal structure of the protein target was obtained by screening the high-resolution structure from the RCSB PDB database [62]. The redundant groups such as water molecules and phosphate were removed by PyMOL 2.6 software, and stored as a PDB format file after pretreatment [63]. AutoDock tool was used to define the hydrogenation, dehydration, charge distribution and rotatable bond of protein and ligand [64], and AutoDock Vina 1.2.5 software was used to carry out molecular docking simulation [65]. The coordinates and size of the docking box were set according to the active pocket of the protein, and the optimal binding conformation was screened by binding free energy scoring. The interaction visualization was performed by Discovery Studio 2019 and PyMOL 2.6 software, and the 2D action diagram and 3D binding pattern diagram was drawn [65].

3.7. Surface plasmon resonance (SPR) experiment

Sensor chip CM5 (Cytiva, Uppsala, Sweden) was used in SPR experiment. After the CM5 chip was loaded, the following operations were performed. Channel activation: an equal volume mixture of 0.4 M EDC and 0.1 M NHS was used to flow through the determination channel at a flow rate of 10 μL/min for 420 s to activate the surface groups on the chip. Ligand coupling: the ligand protein was diluted with 10 mM sodium acetate buffer (pH 4.5) to a final concentration of 50 μg/mL, and the sample was injected at a flow rate of 10 μL/min for 420 s. Channel blocking: 1 M ethanolamine hydrochloride (pH 8.5) was injected at a flow rate of 10 μL/min for 420 s to block the remaining unreacted activated ester groups on the surface. Reference Channel Settings: the reference channel used the same activation and closure procedures, in the coupling phase 10 mM sodium acetate buffer (pH 4.5) without protein was injected at the same flow rate and time as a background subtraction control to eliminate the effects of non-specific binding and solvent volume effects. A 96-well plate was used to dilute

small-molecule compounds for kinetic detection with PBST solution. The initial concentration of TRP was set at 12800 nM, followed by serial dilution to 25 nM; the initial concentration of TLNDs was set at 2048 μg/L, followed by serial dilution to 4 μg/L. All samples of different concentrations were assayed using the Molecular Interaction Analysis System (GE Healthcare, Sweden); the binding time was set to 100 s, and the dissociation time was set to 120 s. At the end of each flow, the chip was regenerated with 10 mM glycine hydrochloride (pH 2.0) solution for 5 min, and the process was repeated until all compounds were measured.

3.8. In vitro experiments

3.8.1. CCK-8 cell viability assay: RSC96 rat Schwann cells were seeded on the first day with 5×10^3 cells per well and incubated for 24 h. Then, concentration gradients of TLNDs (25, 50, 100, and 200 μg/mL), TRP (0.4 mM) and Li_2CO_3 (0.24 mM) were added and further incubated for 24 h. After treatment, 10 μL of CCK-8 solution was added to each well and incubated at 37°C for 1.5 h in the dark. Absorbance at 450 nm was recorded. Viability was calculated as the following equation:

$$[(OD_{experimental}-OD_{blank}) / (OD_{control}-OD_{blank})]\times100\%$$

3.8.2. Calcein-AM/PI live/dead staining: RSC96 cells were pretreated with TLNDs (100 μg/mL), Li_2CO_3 (0.24 mM), or TRP (0.4 mM) for 4 h, and then exposed to 100 μM TBHP for 4 h to assess the cytoprotective effect of TLNDs. Then, all groups of cells were stained with Calcein-AM and propidium iodide (PI) for 20 min at 37°C in the dark. Live (green) and dead (red) cells were visualized under fluorescence microscopy, and the green/red area ratio was quantified using ImageJ.

3.8.3. TLNDs uptake pathway and subcellular distribution: Cells were preincubated for 1 h with 2-deoxy-D-glucose (2-DG, 30 mM, ATP synthesis inhibitor), methyl-β-cyclodextrin (M-β-CD, 2 mM, lipid raft disruptor), amiloride (AMI, 100 μM, macropinocytosis inhibitor), genistein (GEN, 200 μM, caveolae/vesicle endocytosis inhibitor), or chlorpromazine (CPZ, 10 μM, clathrin-mediated endocytosis inhibitor).

After 4 h of incubation with TLNDs (100 μg/mL), cells were stained with Mito-Tracker, Lyso-Tracker, or ER-Tracker for 30 min at 37°C. Confocal microscopy was used to capture images.

3.8.4. Staining with several fluorescent probes: After the indicated treatments, RSC96 cells were stained with DCFH-DA (10 μM, 30 min) for total ROS, MitoSOX^{TM} Red (5 μM, 15 min) for mitochondrial superoxide, Lyso-Tracker Red (50 nM, 30 min) for lysosomes, and JC-10 (5 μM, 20 min) for mitochondrial membrane potential. For lipid droplets and cholesterol, cells were fixed and stained with BODIPY 493/503 (1 μg/mL) and NBD-cholesterol (5 μM), respectively. Cell boundaries were labeled with CellMask^{TM} Deep Red (5 μg/mL), and ferrous iron was detected using a specific Fe^{2+} probe. All fluorescence images were captured using a confocal microscope (Olympus), and the fluorescence intensity was quantified using ImageJ software. All imaging parameters were kept constant across treatment groups for valid comparisons.

3.8.5. The measurements of biochemical substances and inflammatory cytokines: RSC96 cells were lysed for the measurement of SOD, MDA, GSH, and ATP using commercial kits according to the manufacturers' instructions. All values were normalized to total protein content determined by the BCA assay. In parallel, the levels of TNF-α, IL-1β, IL-6, and CTSB in the cell culture supernatants were assessed by ELISA kits, with each sample run in triplicate.

3.8.6. Western blotting: For the extraction of proteins, RIPA buffer with protease and phosphatase inhibitors was used. After resolution on 10% SDS-PAGE, proteins were transferred onto PVDF membranes. Membranes were blocked with 10% FBS for 2 h at room temperature, and then incubated with primary antibodies overnight at 4°C, followed by HRP-conjugated secondary antibodies for 2 h at room temperature. We used Tecan apparatus to analyze luminescence signals. Table S1 lists the details of the antibodies.

3.8.7. Cellular thermal shift assay (CETSA): RSC96 cells were incubated with 100 μg/mL TLNDs or PBS for 4 h at 37°C. The cells were then heated in a PCR thermal cycler from 35 to 62°C, with each temperature held for 3 min. Soluble proteins were extracted by repeated freeze–thaw cycles in liquid nitrogen, and IDO1 levels were assessed by Western blotting. Band intensities were quantified to generate melting curves and calculate T_m values.

3.8.8. Enzymatic activity assay for IDO1: The Recombinant human IDO1 protein was dissolved in the IDO1 assay buffer-50 mM potassium phosphate buffer, pH 6.5, containing 25 mM neutralized ascorbic acid, 10 μM methylene blue and 100 μg/mL catalase in a final concentration of 25 μg/mL. The reaction mixture (100 μL) consisted of the enzyme solution with 200 μM L-tryptophan substrate and different concentrations of TLNDs (0, 0.78, 1.56, 3.125, 6.25, 12.5, 25, 50, 100, 200 μg/mL) and incubated at 37°C for 60 min. Eapacodast (10 μM) was used as a positive control. Upon incubation, 10 μL of 1 M NaOH was added and kept at 60 °C for 30 min to hydrolyze N-Formylkynurenine to Kynurenine. The sample was kept on ice and then centrifuged for 10 min at 12,000 rpm. Next, 100 μL of the supernatant was mixed with an equal volume of 2% (w/v) p-dimethylaminobenzaldehyde (Ehrlich's reagent) in acetic acid, incubated at room temperature for 10 min, and the absorbance was measured at 480 nm [66].

3.8.9. Construction of IDO1-overexpressing RSC96 stable cell line: Lentiviral vectors carrying the rat IDO1 full-length coding sequence (LV-IDO1) or a negative control (LV-NC) were obtained from Shanghai Sangon Biotech Co., Ltd. Stable lines were generated following a published protocol [67]. RSC96 cells were transduced with LV-IDO1 or LV-NC in the presence of 5 μg/mL polybrene, and selection was performed with 2 μg/mL puromycin for 10 days, after which cells were maintained in 1 μg/mL puromycin. Overexpression was verified by Western blotting.

3.9. In vivo experiments

3.9.1. Model of sciatic nerve crush injury in rat: Changchun Yiyuan Biotechnology supplied male SD rats of 200-220 g aged 6-8 weeks. Approval for all animal experiments was granted by Institutional Animal Care and Use Committee (IACUC) of the School of Public Health, Jilin University (2026-07-001) and strictly adhered to all NIH regulations. Under anesthesia, the right sciatic nerve was exposed and crushed twice with a non-traumatic vascular clamp, each crush lasting 30 s with a 10 s interval. Buprenorphine (0.05 mg/kg) was administered subcutaneously after surgery. Drugs (20 μL) diluted by sterilized PBS were injected locally beneath the epineurium, including PBS, TLNDs (2.5 mg/mL), Li_2CO_3 (0.5 mg/mL), or TRP (2 mg/mL).

3.9.2. Safety and organ toxicity in an organism: For a period of 14 days, TLNDs were injected daily at 10, 20, or 40 mg/kg in rats. Blood samples were collected on days 7, 14, and 28 for the assessment of AST, ALT, ALP, and BUN. Histological analysis was performed on fixed, sectioned, and hematoxylin-and-eosin-stained (H&E) sections of internal organs.

3.9.3. Footprint gait analysis: Footprint analysis was performed at 7,14, and 28 days after surgery to assess hindlimb motor function. After ink application to the hind paws, rats were allowed to walk along a paper-lined track, and the footprints were recorded. The Sciatic Function Index (SFI) was calculated based on toe spread (TS: distance between the first and fifth toes), print length (PL: total footprint length), and intermediate toe spread (IT: distance between the second and fourth toes) using the standard formula [68], with E indicating the injured side and N the normal side.

$$SFI=-38.3\left[\frac{EPL-NPL}{NPL}\right]+109.5\left[\frac{ETS-NTS}{NTS}\right]+13.3\left[\frac{EIT-NIT}{NIT}\right]-8.8$$

3.9.4. Neuroelectrophysiology: CMAPs were elicited from the gastrocnemius muscle in rats anesthetized with isoflurane, using a Keypoint electromyography system (Neurolite AG, Brunnen, Switzerland). After surgical exposure of the sciatic nerve, a pair of needle electrodes—the recording electrode and the reference electrode—were

inserted into the muscle belly and the corresponding tendon, respectively. A stimulating electrode was gently placed on the epineurial surface of the sciatic nerve, approximately 2 mm proximal to the injury site. CMAP amplitudes were recorded in response to a single electrical stimulus of 5.0 mA intensity. All recordings were performed under consistent conditions, and the maximal peak-to-peak amplitude was measured.

3.9.5. Muscle atrophy detection: On postoperative day 28, bilateral gastrocnemius muscles were harvested from each rat and immediately weighed using an electronic analytical balance (Mettler Toledo, Greifensee, Switzerland). Muscle atrophy was quantified as the wet weight ratio of the injured side to the uninjured side. For Masson's trichrome staining, mid-belly muscle specimens were fixed in 4% paraformaldehyde, embedded in paraffin, and transversely sectioned at 5 μm thickness. Following deparaffinization and rehydration, the sections were stained using a Masson's trichrome stain kit according to the manufacturer's protocol, and images were captured under a light microscope (Olympus). The myofiber cross-sectional area was measured in three randomly selected fields per section using ImageJ software (NIH, Bethesda, MD, USA).

3.9.6. Toluidine blue staining (TBS) and transmission electron microscopy (TEM): Semi-thin nerve sections were stained with toluidine blue. Ultra-thin sections were double-stained with uranyl acetate and lead citrate. Myelin architecture was examined by light microscopy and TEM; myelinated fiber numbers and myelin thickness were quantified.

3.9.7. Immunohistochemistry and immunofluorescence: Paraffin-embedded sections were dewaxed, subjected to antigen retrieval, permeabilized with 0.5% Triton, and blocked with 10% FBS for 2 h at room temperature. Primary antibodies were applied overnight at 4°C, followed by secondary antibodies. For immunohistochemistry (IHC), DAB staining with hematoxylin counterstaining was performed. For immunofluorescence (IF), fluorescent secondary antibodies were used, and nuclei were counterstained with DAPI. Images were acquired with an Olympus confocal

microscope. Antibodies are listed in Table S1.

3.9.8. Detection of TRP metabolites in sciatic nerve: Tissue samples were collected and analyzed by UPLC-MS/MS (Wuhan Maiwei Metabolism Biotechnology Co., Ltd.). Specimens were frozen-thawed in liquid nitrogen, extracted with methanol, and quantified using internal standards. ESI-MRM mode was employed, and concentrations were derived from standard curves.

3.10. DRG explant culture and immunofluorescence: Dorsal root ganglia (DRGs) from newborn SD rats were isolated, embedded in Matrigel with serum-free medium, and cultured at 37°C in 5% CO_2. After permeabilization and blocking, explants were incubated with β-Tubulin at 4°C. Images were taken by confocal microscopy.

3.11. Statistical analysis: Data were analyzed using GraphPad Prism 9.5 and are expressed as mean ± standard deviation (SD). Two-group comparisons were performed with two-tailed unpaired t-tests; multiple groups were compared by one- or two-way ANOVA and Tukey's test. A value of $p<0.05$ was considered statistically significant.

4. Conclusion

In summary, we established that IDO1-driven TRP metabolic disorders and the transformation to the neurotoxic kynurenine-QUIN axis are the core pathological drivers of SCs dysfunction after PNI. Based on the thought of ‘competition from the same origin’, novel tryptophan-Li^+ carbon dots (TLNDs) were designed, which can competitively occupy the IDO1 active pocket confirmed by SPR and molecular docking simulation. These biomimetic nano-inhibitor platforms that retained the enzyme recognition characteristic groups but did not participate in or disrupt primitive amino acid metabolism might be extended to other types of essential amino acids. The TLNDs-treated SCs effectively reversed the above cascade process and led to subsequent multifaceted results, including up-regulation of SLC7A11, GPX4 and ferritin, activation of the NRF2-HO1 antioxidant axis, and inhibition of ferroptosis. Meanwhile,

TLNDs promoted TFEB nuclear translocation, restored lysosomal biosynthesis and lipophagy in SCs, and improved cholesterol transporters of NPC1, NPC2 and ABCG1. Crucially, IDO1 overexpression completely abolished all the protective effects, confirming that IDO1 is an essential upstream target of TLNDs. Finally, the therapeutic potential of TLNDs was verified in a rat sciatic nerve injury model, in which the nerve conduction and the myelin regeneration were significantly accelerated by subepineurial injection of TLNDs. In general, this work established IDO1-mediated TRP metabolism as a previously unrecognized therapeutic target in PNI, opening up a paradigm from traditional anti-inflammatory strategies to metabolic recovery of SCs organelles. In addition to traumatic nerve injury, the IDO1-KYN axis is also dysregulated in diabetic neuropathy and neuropathic pain, suggesting that the IDO1 nano-inhibitors reported in this study has broad applicability and provides a conceptual basis for the treatment of nerve diseases.

Acknowledgements

Not applicable.

Funding

This work was supported by the Jilin Provincial Natural Science Foundation (No. YDZJ202601ZYTS638, YDZJ202501ZYTS039), the National Natural Science Foundation (NSFC; under Grant No. 82401607), the Jilin Provincial Special Project for Medical and Health Talents (No. JLSRCZX2026-63, JLSRCZX2026-36), the Bethune Project of Jilin University (No. 2026B05) and Talent Reserve Program of The First Hospital of Jilin University (No. JDYY-TRP-2024005).

Data availability

The data that support the findings of this study are available from the corresponding authors upon reasonable request.

Authorship contributions

Xin Yu: Writing-review & editing, Writing-original draft, Visualization, Project administration, Methodology, Investigation, Formal analysis, Data curation, Conceptualization, Funding acquisition. **Jingyan Ren:** Writing-review & editing, Investigation, Data curation. **Zhenghang Li:** Visualization, Methodology, Investigation, Data curation. **Wenjun Yu:** Methodology, Investigation, Formal analysis, Data curation. **Jie Zhang:** Visualization, Validation, Methodology, Investigation, Formal analysis, Data curation. **Deer Yi:** Validation, Investigation, Data curation. **Qidong Shi:** Visualization, Investigation, Data curation. **Laijin Lu:** Supervision, Resources, Conceptualization. **Bin Liu:** Supervision, Resources, Conceptualization. **Mingxi Yang:** Writing-review & editing, Writing-original draft, Visualization, Methodology, Investigation, Formal analysis, Data curation, Conceptualization.

Ethics approval and consent to particitate

All animal experiments adhered to strict animal welfare guidelines and were approved by the Institutional Animal Care and Use Committee (IACUC) of the School of Public Health, Jilin University (2026-07-001).

Consent for publication

All authors have read and approved the final manuscript and consent to its publication.

Competing interests

The authors declare that they have no competing interests.

References

(1) Liu, Z. G.; Zou, Y. L.; Zhang, M. X.; Yang, F.; Li, P. F.; Zhang, B. Y. Revisiting the Peripheral Nerve Injury and Regeneration. *Neuromolecular Med* **2026**, *28* (1). DOI: 10.1007/s12017-026-08914-z From NLM Medline.

(2) Robinson, L. R. Traumatic injury to peripheral nerves. *Muscle Nerve* **2022**, *66* (6), 661–670. DOI: 10.1002/mus.27706 From NLM Medline.

(3) Zhang, X.; Zhang, Y.; Chen, Y.; Ji, Y.; Lyu, Y.; Miao, Z.; Duan, X.; Liu, X. Unraveling the immune system's role in peripheral nerve regeneration: a pathway to enhanced healing. *Front Immunol* **2025**, *16*, 1540199. DOI: 10.3389/fimmu.2025.1540199 From NLM Medline.

(4) Waller, T. J.; Collins, C. A.; Dus, M. Pyruvate kinase deficiency links metabolic perturbations to neurodegeneration and axonal protection. *Mol Metab* **2025**, *98*, 102187. DOI: 10.1016/j.molmet.2025.102187 From NLM Medline.

(5) Merlini, E.; Coleman, M. P.; Loreto, A. Mitochondrial dysfunction as a trigger of programmed axon death. *Trends Neurosci* **2022**, *45* (1), 53–63. DOI: 10.1016/j.tins.2021.10.014 From NLM Medline.

(6) Virdee, S. An atypical ubiquitin ligase at the heart of neural development and programmed axon degeneration. *Neural Regen Res* **2022**, *17* (11), 2347–2350. DOI: 10.4103/1673-5374.338992 From NLM PubMed-not-MEDLINE.

(7) Li, B.; Zhang, Z.; Wang, H.; Zhang, D.; Han, T.; Chen, H.; Chen, J.; Chen, Z.; Xie, Y.; Wang, L.; et al. Melatonin promotes peripheral nerve repair through Parkin-mediated mitophagy. *Free Radic Biol Med* **2022**, *185*, 52–66. DOI: 10.1016/j.freeradbiomed.2022.04.016 From NLM Medline.

(8) Martellucci, S.; Heredia, M.; Wang, Z.; Whisenant, T.; Strickland, D. K.; Sanchez, R.; Arai, T.; Zhang, M.; Wang, H.; Gong, Z.; et al. The low-density lipoprotein receptor-related protein-1 (LRP1) in Schwann cells controls mitochondria homeostasis in peripheral nerves. *Prog Neurobiol* **2025**, *251*, 102796. DOI: 10.1016/j.pneurobio.2025.102796 From NLM Medline.

(9) Wen, S.; Zou, Z. R.; Cheng, S.; Guo, H.; Hu, H. S.; Zeng, F. Z.; Mei, X. F. Ginsenoside Rb1 improves energy metabolism after spinal cord injury. *Neural Regen Res* **2023**, *18* (6), 1332–1338. DOI: 10.4103/1673-5374.357915 From NLM PubMed-not-MEDLINE.

(10) Wu, Z.; Yan, W.; Wang, K.; Xu, G.; Zhu, D.; Li, X.; Wang, H.; Yang, M.; Zhang, X.; Wu, J. Lysosomal dysfunction in Schwann cells is involved in bortezomib-induced peripheral neurotoxicity. *Arch Toxicol* **2023**, *97* (5), 1385–1396. DOI: 10.1007/s00204-023-03468-6 From NLM Medline.

(11) Yan, W.; Chen, Y.; Wu, H.; Gao, Z.; Hu, X.; Ao, Y.; Mao, C.; Wan, M. Artificial mitochondria ameliorates osteoarthritis through restoring cellular energy metabolism homeostasis. *Bioact Mater* **2026**, *61*, 940–966. DOI: 10.1016/j.bioactmat.2026.02.028 From NLM PubMed-not-MEDLINE.

(12) Yan, Y.; Li, Y.; Ma, H. Mitochondria-lysosome contacts in aging: A mechanistic interface linking organelle homeostasis and cellular decline. *Mech Ageing Dev* **2026**, *231*, 112191. DOI: 10.1016/j.mad.2026.112191 From NLM Medline.

(13) Qin, W.; Shi, Y.; Chen, W.; Jia, X.; Asakawa, T. Can kynurenine pathway be considered as a next-generation therapeutic target for Parkinson's disease? An update information. *Biosci Trends* **2022**, *16* (4), 249–256. DOI: 10.5582/bst.2022.01352 From NLM Medline.

(14) Gao, J.; Yang, T.; Song, B.; Ma, X.; Ma, Y.; Lin, X.; Wang, H. Abnormal tryptophan catabolism in diabetes mellitus and its complications: Opportunities and challenges. *Biomed Pharmacother* **2023**, *166*, 115395. DOI: 10.1016/j.biopha.2023.115395 From NLM Medline.

(15) Pocivavsek, A.; Schwarcz, R.; Erhardt, S. Neuroactive Kynurenines as Pharmacological Targets:

New Experimental Tools and Exciting Therapeutic Opportunities. *Pharmacol Rev* **2024**, *76* (6), 978–1008. DOI: 10.1124/pharmrev.124.000239 From NLM Medline.
(16) Huang, Y.; Zhao, M.; Chen, X.; Zhang, R.; Le, A.; Hong, M.; Zhang, Y.; Jia, L.; Zang, W.; Jiang, C.; et al. Tryptophan Metabolism in Central Nervous System Diseases: Pathophysiology and Potential Therapeutic Strategies. *Aging Dis* **2023**, *14* (3), 858–878. DOI: 10.14336/AD.2022.0916 From NLM PubMed-not-MEDLINE.
(17) Yan, D.; Lin, Y. W.; Tan, X. Heme-containing enzymes and inhibitors for tryptophan metabolism. *Metallomics* **2017**, *9* (9), 1230–1240. DOI: 10.1039/c7mt00105c From NLM Medline.
(18) Opitz, C. A.; Somarribas Patterson, L. F.; Mohapatra, S. R.; Dewi, D. L.; Sadik, A.; Platten, M.; Trump, S. The therapeutic potential of targeting tryptophan catabolism in cancer. *Br J Cancer* **2020**, *122* (1), 30–44. DOI: 10.1038/s41416-019-0664-6 From NLM Medline.
(19) Labadie, B. W.; Bao, R.; Luke, J. J. Reimagining IDO Pathway Inhibition in Cancer Immunotherapy via Downstream Focus on the Tryptophan-Kynurenine-Aryl Hydrocarbon Axis. *Clin Cancer Res* **2019**, *25* (5), 1462–1471. DOI: 10.1158/1078-0432.CCR-18-2882 From NLM Medline.
(20) Zhu, H.; Yang, Y. S.; Zhu, L. Y.; Jiang, C. R.; Zhang, Z.; Xu, M. T.; Li, R. T.; Ye, R. R. Iridium(III)/rhenium(I) complexes bearing NLG919 as the ligand for enhanced triple-negative breast cancer therapy. *Dalton Trans* **2025**, *54* (39), 14962–14968. DOI: 10.1039/d5dt01732g From NLM Medline.
(21) Li, S.; Yue, Y.; Du, J.; Zhao, W.; Liu, B.; Ma, Z.; Wang, X.; Wei, Y.; Song, C.; Zhang, G. Carrier-free nanoreshapers disrupt cancer-associated fibroblast barriers and alleviate immunosuppression for synergistically potentiated immunotherapy. *J Control Release* **2026**, *393*, 114835. DOI: 10.1016/j.jconrel.2026.114835 From NLM Medline.
(22) Guo, Y.; Liu, Y.; Wu, W.; Ling, D.; Zhang, Q.; Zhao, P.; Hu, X. Indoleamine 2,3-dioxygenase (Ido) inhibitors and their nanomedicines for cancer immunotherapy. *Biomaterials* **2021**, *276*, 121018. DOI: 10.1016/j.biomaterials.2021.121018 From NLM Medline.
(23) Karahan, H.; Hartigan, K.; Al-Amin, M. M.; John, S. K.; McCord, B.; Wijeratne, H. R. S.; Acri, D. J.; Smith, D. C.; Dabin, L. C.; Cordero, H. M. R.; et al. Deletion of neuronal Idol ameliorates Alzheimer's disease-related pathologies via APOE receptors. *Alzheimers Dement* **2025**, *21* (12), e70949. DOI: 10.1002/alz.70949 From NLM Medline.
(24) Ethordevic, L.; Arcudi, F.; Cacioppo, M.; Prato, M. A multifunctional chemical toolbox to engineer carbon dots for biomedical and energy applications. *Nat Nanotechnol* **2022**, *17* (2), 112–130. DOI: 10.1038/s41565-021-01051-7 From NLM Medline.
(25) Liu, Y.; Zhang, L.; Cai, H.; Qu, X.; Chang, J.; Waterhouse, G. I. N.; Lu, S. Biomass-derived carbon dots with pharmacological activity for biomedicine: Recent advances and future perspectives. *Sci Bull (Beijing)* **2024**, *69* (19), 3127–3149. DOI: 10.1016/j.scib.2024.08.011 From NLM Medline.
(26) Li, Y.; Huang, X.; Qiao, Q.; Li, Y.; Han, X.; Chen, C.; Chen, Y.; Guo, S.; Zhang, Y.; Gao, W.; et al. Suppression of Sepsis Cytokine Storm by Escherichia Coli Cell Wall-Derived Carbon Dots. *Adv Mater* **2025**, *37* (12), e2414237. DOI: 10.1002/adma.202414237 From NLM Medline.
(27) Jia, Z.; Wang, C.; Han, X.; Zeng, J.; He, C.; Chen, Z.; Chen, Y.; Xu, B. Targeting the HIF-1alpha/PPARgamma axis with curcumin carbon dots to combat uranium nephrotoxicity. *J Nanobiotechnology* **2026**, *24* (1). DOI: 10.1186/s12951-026-04620-x From NLM Medline.
(28) Wei, C.; Cheng, S.; Zhang, Y.; Zhao, Y.; Wei, H.; Wang, F.; Wang, J. H.; Jiang, D.; Wang, Z. A liver-targeting fluorescent nano-drug for theranostics in non-alcoholic fatty liver disease.

Biomaterials **2026**, *333*, 124182. DOI: 10.1016/j.biomaterials.2026.124182 From NLM Medline.
(29) Yang, M.; Su, B.; Ma, Z.; Zheng, X.; Liu, Y.; Li, Y.; Ren, J.; Lu, L.; Yang, B.; Yu, X. Renal-friendly Li(+)-doped carbonized polymer dots activate Schwann cell autophagy for promoting peripheral nerve regeneration. *Acta Biomater* **2023**, *159*, 353–366. DOI: 10.1016/j.actbio.2023.01.027 From NLM Medline.
(30) Zhu, J. Y.; Ni, X. S.; Han, X. Y.; Liu, S.; Ji, Y. K.; Yao, J.; Yan, B. Metabolomic profiling of a neurodegenerative retina following optic nerve transection. *Mol Med Rep* **2023**, *28* (3). DOI: 10.3892/mmr.2023.13065 From NLM Medline.
(31) Ala, M.; Mohammad Jafari, R.; Aghajanpour, L.; Sanatkar, M.; Aghsaei Fard, M.; Goudarzi, S.; Shadboorestan, A.; Dehpour, A. R. Protective effects of sumatriptan against optic nerve injury in rats via modulation of kynurenine pathway, oxidative stress and apoptosis. *Bioimpacts* **2025**, *15*, 30409. DOI: 10.34172/bi.30409 From NLM PubMed-not-MEDLINE.
(32) Li, X.; Meng, H.; Wang, H.; Zhang, Y.; Yu, W. Indoleamine 2,3-dioxygenase 1 in cancer immunotherapy: from small-molecule inhibition to PROTAC-mediated degradation. *Front Pharmacol* **2025**, *16*, 1640073. DOI: 10.3389/fphar.2025.1640073 From NLM PubMed-not-MEDLINE.
(33) Savonije, K.; Meek, A.; Weaver, D. F. Indoleamine 2,3-Dioxygenase as a Therapeutic Target for Alzheimer's Disease and Geriatric Depression. *Brain Sci* **2023**, *13* (6). DOI: 10.3390/brainsci13060852 From NLM PubMed-not-MEDLINE.
(34) Wang, Z.; Li, L.; Dong, Y.; Zhang, Y. The microbiota-tryptophan-brain axis in neurodegenerative diseases: pathogenic mechanisms, disease-specific roles, and translational therapeutics. *Front Microbiol* **2026**, *17*, 1820111. DOI: 10.3389/fmicb.2026.1820111 From NLM PubMed-not-MEDLINE.
(35) Nguyen, R. C.; Shin, I.; Liu, A. Deciphering Tryptophan Oxygenation: Key Modulators of 2-Oxindole Formation in MarE. *Angew Chem Int Ed Engl* **2025**, *64* (35), e202510848. DOI: 10.1002/anie.202510848 From NLM Medline.
(36) Makoukji, J.; Belle, M.; Meffre, D.; Stassart, R.; Grenier, J.; Shackleford, G.; Fledrich, R.; Fonte, C.; Branchu, J.; Goulard, M.; et al. Lithium enhances remyelination of peripheral nerves. *Proc Natl Acad Sci U S A* **2012**, *109* (10), 3973–3978. DOI: 10.1073/pnas.1121367109 From NLM Medline.
(37) Snitow, M. E.; Bhansali, R. S.; Klein, P. S. Lithium and Therapeutic Targeting of GSK-3. *Cells* **2021**, *10* (2). DOI: 10.3390/cells10020255 From NLM Medline.
(38) Wang, W. L.; Jia, Z. Z.; Deng, Z. C.; Zhu, Y. Y.; Xu, C. X.; Dong, G. M.; Gao, B. W.; Fu, J. L.; Zhang, S. L.; Chen, L. Y.; et al. 5-Aminosalicylic Acid-Derived Carbon Dots Nanozyme for Ulcerative Colitis Treatment via Inhibiting NF-κB/AGE-RAGE Pathway and Modulating Arachidonic Acid Metabolism. *Adv Funct Mater* **2026**. DOI: 10.1002/adfm.202527665.
(39) Wei, Y. Y.; Chen, L.; Wang, J. L.; Liu, X. G.; Yang, Y. Z.; Yu, S. P. Investigation on the chirality mechanism of chiral carbon quantum dots derived from tryptophan. *Rsc Adv* **2019**, *9* (6), 3208–3214. DOI: 10.1039/c8ra09649j.
(40) Wang, D.; He, T. W.; Li, S. S.; Jiang, Y. Z.; Yuan, M. J. Li-Doped Chemical Bath Deposited SnO Enables Efficient Perovskite Photovoltaics. *Acs Appl Energ Mater* **2022**, *5* (5), 5340–5347. DOI: 10.1021/acsaem.1c02666.
(41) Ramanathan, A. Toxicity of nanoparticles_ challenges and opportunities. *Appl Microsc* **2019**, *49* (1), 2. DOI: 10.1007/s42649-019-0004-6 From NLM PubMed-not-MEDLINE.
(42) Oksel Karakus, C.; Bilgi, E.; Winkler, D. A. Biomedical nanomaterials: applications, toxicological

concerns, and regulatory needs. *Nanotoxicology* **2021**, *15* (3), 331–351. DOI: 10.1080/17435390.2020.1860265 From NLM Medline.
(43) Chakraborty, A.; Jana, N. R. Clathrin to Lipid Raft-Endocytosis via Controlled Surface Chemistry and Efficient Perinuclear Targeting of Nanoparticle. *J Phys Chem Lett* **2015**, *6* (18), 3688–3697. DOI: 10.1021/acs.jpclett.5b01739 From NLM Medline.
(44) Mrksich, K.; Padilla, M. S.; Mitchell, M. J. Breaking the final barrier: Evolution of cationic and ionizable lipid structure in lipid nanoparticles to escape the endosome. *Adv Drug Deliv Rev* **2024**, *214*, 115446. DOI: 10.1016/j.addr.2024.115446 From NLM Medline.
(45) Qiu, C.; Xia, F.; Zhang, J.; Shi, Q.; Meng, Y.; Wang, C.; Pang, H.; Gu, L.; Xu, C.; Guo, Q.; et al. Advanced Strategies for Overcoming Endosomal/Lysosomal Barrier in Nanodrug Delivery. *Research (Wash D C)* **2023**, *6*, 0148. DOI: 10.34133/research.0148 From NLM PubMed-not-MEDLINE.
(46) Halawani, D.; Wang, Y.; Li, J.; Halperin, D.; Ni, H.; Estill, M.; Ramakrishnan, A.; Shen, L.; Sefiani, A.; Geoffroy, C. G.; et al. AhR inhibition promotes axon regeneration via a stress-growth switch. *Nature* **2026**, *653* (8116), 1119–1129. DOI: 10.1038/s41586-026-10295-z From NLM Medline.
(47) Goncalves, M.; Rodrigues-Santos, P.; Januario, C.; Cosentino, M.; Pereira, F. C. Indoleamine 2,3-dioxygenase (IDO1) - Can dendritic cells and monocytes expressing this moonlight enzyme change the phase of Parkinson's Disease? *Int Immunopharmacol* **2024**, *133*, 112062. DOI: 10.1016/j.intimp.2024.112062 From NLM Medline.
(48) An, X.; Li, C.; Chai, Y.; Wang, H.; Yang, L.; Qin, L.; Soprun, L. A.; Gavrilova, N. Y.; Wen, Z.; Xu, J.; et al. Luteolin rescues high-fat diet-induced hippocampal mitochondrial oxidative stress and cognitive decline by regulating gut microbiota-kynurenine-aryl hydrocarbon receptor axis. *Free Radic Biol Med* **2026**, *253*, 427–442. DOI: 10.1016/j.freeradbiomed.2026.06.002 From NLM Publisher.
(49) Li, Y.; Munoz-Mayorga, D.; Nie, Y.; Kang, N.; Tao, Y.; Lagerwall, J.; Pernaci, C.; Curtin, G.; Coufal, N. G.; Mertens, J.; et al. Microglial lipid droplet accumulation in tauopathy brain is regulated by neuronal AMPK. *Cell Metab* **2024**, *36* (6), 1351–1370 e1358. DOI: 10.1016/j.cmet.2024.03.014 From NLM Medline.
(50) Tan, Z.; Hu, H.; Chen, H.; Lin, Y.; Zhou, M.; Zhang, W.; Xu, P.; Chen, X. Transaldolase 1 impacts Parkinson's disease pathogenesis via metabolic reprogramming and autophagy-lysosomal pathway. *Acta Neuropathol Commun* **2025**, *13* (1), 223. DOI: 10.1186/s40478-025-02133-6 From NLM Medline.
(51) Jeong, S. J.; Stitham, J.; Evans, T. D.; Zhang, X.; Rodriguez-Velez, A.; Yeh, Y. S.; Tao, J.; Takabatake, K.; Epelman, S.; Lodhi, I. J.; et al. Trehalose causes low-grade lysosomal stress to activate TFEB and the autophagy-lysosome biogenesis response. *Autophagy* **2021**, *17* (11), 3740–3752. DOI: 10.1080/15548627.2021.1896906 From NLM Medline.
(52) Saher, G.; Quintes, S.; Nave, K. A. Cholesterol: a novel regulatory role in myelin formation. *Neuroscientist* **2011**, *17* (1), 79–93. DOI: 10.1177/1073858410373835 From NLM Medline.
(53) Pfeffer, S. R. NPC intracellular cholesterol transporter 1 (NPC1)-mediated cholesterol export from lysosomes. *J Biol Chem* **2019**, *294* (5), 1706–1709. DOI: 10.1074/jbc.TM118.004165 From NLM Medline.
(54) Yu, T.; Lieberman, A. P. Npc1 acting in neurons and glia is essential for the formation and maintenance of CNS myelin. *PLoS Genet* **2013**, *9* (4), e1003462. DOI: 10.1371/journal.pgen.1003462 From NLM Medline.

(55) Tan, R.; Zhang, K.; Si, Y.; Huang, K.; Jia, W.; Li, M.; Iqbal, S.; Zhang, S.; Zhai, Z.; Hu, J. Multi-functional self-powered nanofiber conduit for peripheral nerve regeneration and muscle atrophy prevention. *J Nanobiotechnology* **2026**, *24* (1). DOI: 10.1186/s12951-026-04241-4 From NLM Medline.
(56) Zhang, L.; Ma, Z.; Smith, G. M.; Wen, X.; Pressman, Y.; Wood, P. M.; Xu, X. M. GDNF-enhanced axonal regeneration and myelination following spinal cord injury is mediated by primary effects on neurons. *Glia* **2009**, *57* (11), 1178–1191. DOI: 10.1002/glia.20840 From NLM Medline.
(57) Rahman, A. U.; Santana, R. C.; de Pinho Pereira, M. M.; Moura, C.; da Silva, D. S.; Araujo, O. C.; Leal-Calvo, T.; Espasandin, I.; da Silva, T. P.; Sarno, E. N.; et al. IDO-Mediated Immune and Metabolic Dysregulation in Schwann Cells Exposed to Mycobacterium leprae. *Cells* **2025**, *14* (19). DOI: 10.3390/cells14191550 From NLM Medline.
(58) Sodhi, R. K.; Bansal, Y.; Singh, R.; Saroj, P.; Bhandari, R.; Kumar, B.; Kuhad, A. IDO-1 inhibition protects against neuroinflammation, oxidative stress and mitochondrial dysfunction in 6-OHDA induced murine model of Parkinson's disease. *Neurotoxicology* **2021**, *84*, 184–197. DOI: 10.1016/j.neuro.2021.03.009 From NLM Medline.
(59) Kuffler, D. P. Can lithium enhance the extent of axon regeneration and neurological recovery following peripheral nerve trauma? *Neural Regen Res* **2022**, *17* (5), 948–952. DOI: 10.4103/1673-5374.324830 From NLM PubMed-not-MEDLINE.
(60) Palomo Irigoyen, M.; Tamayo Caro, M.; Perez Andres, E.; Barreira Manrique, A.; Varela Rey, M.; Woodhoo, A. Isolation and Purification of Primary Rodent Schwann Cells. *Methods Mol Biol* **2018**, *1791*, 81–93. DOI: 10.1007/978-1-4939-7862-5_7 From NLM Medline.
(61) Hai, M.; Muja, N.; DeVries, G. H.; Quarles, R. H.; Patel, P. I. Comparative analysis of Schwann cell lines as model systems for myelin gene transcription studies. *J Neurosci Res* **2002**, *69* (4), 497–508. DOI: 10.1002/jnr.10327 From NLM Medline.
(62) Berman, H. M.; Westbrook, J.; Feng, Z.; Gilliland, G.; Bhat, T. N.; Weissig, H.; Shindyalov, I. N.; Bourne, P. E. The Protein Data Bank. *Nucleic Acids Res* **2000**, *28* (1), 235–242. DOI: 10.1093/nar/28.1.235 From NLM Medline.
(63) DeLano, W. L. PyMOL molecular viewer: Updates and refinements. *Abstr Pap Am Chem S* **2009**, *238*.
(64) Morris, G. M.; Huey, R.; Lindstrom, W.; Sanner, M. F.; Belew, R. K.; Goodsell, D. S.; Olson, A. J. AutoDock4 and AutoDockTools4: Automated docking with selective receptor flexibility. *J Comput Chem* **2009**, *30* (16), 2785–2791. DOI: 10.1002/jcc.21256 From NLM Medline.
(65) Trott, O.; Olson, A. J. AutoDock Vina: improving the speed and accuracy of docking with a new scoring function, efficient optimization, and multithreading. *J Comput Chem* **2010**, *31* (2), 455–461. DOI: 10.1002/jcc.21334 From NLM Medline.
(66) Xu, X.; Ren, J.; Ma, Y.; Liu, H.; Rong, Q.; Feng, Y.; Wang, Y.; Cheng, Y.; Ge, R.; Li, Z.; et al. Discovery of cyanopyridine scaffold as novel indoleamine-2,3-dioxygenase 1 (IDO1) inhibitors through virtual screening and preliminary hit optimisation. *J Enzyme Inhib Med Chem* **2019**, *34* (1), 250–263. DOI: 10.1080/14756366.2018.1480614 From NLM Medline.
(67) Wang, F.; Liu, L.; Wang, J.; Liu, M.; Zhang, W.; Zhao, L.; Zhai, C.; Xu, Y. Gain-of-function of IDO in DCs inhibits T cell immunity by metabolically regulating surface molecules and cytokines. *Exp Ther Med* **2023**, *25* (5), 234. DOI: 10.3892/etm.2023.11933 From NLM PubMed-not-MEDLINE.
(68) Bain, J. R.; Mackinnon, S. E.; Hunter, D. A. Functional evaluation of complete sciatic, peroneal, and posterior tibial nerve lesions in the rat. *Plast Reconstr Surg* **1989**, *83* (1), 129–138. DOI:

10.1097/00006534-198901000-00024 From NLM Medline.

Supplementary Files

This is a list of supplementary files associated with this preprint. Click to download.

- Supplementarymaterial.docx